# Gravitational-wave echoes from numerical-relativity waveforms via spacetime construction near merging compact objects

Sizheng Ma,[1,*] Qingwen Wang,[2] Nils Deppe,[1] François Hébert,[1] Lawrence E. Kidder,[3] Jordan Moxon,[1] William Throwe,[3] Nils L. Vu,[4] Mark A. Scheel,[1] and Yanbei Chen[1,†]

[1]*Theoretical Astrophysics 350-17, California Institute of Technology, Pasadena, California 91125, USA*
[2]*Perimeter Institute and University of Waterloo, Waterloo, Ontario N2L 2Y5, Canada*
[3]*Cornell Center for Astrophysics and Planetary Science, Cornell University, Ithaca, New York 14853, USA*
[4]*Max Planck Institute for Gravitational Physics (Albert Einstein Institute), Am Mühlenberg 1, D-14476 Potsdam, Germany*

(Received 7 March 2022; accepted 20 April 2022; published 5 May 2022)

We propose a new approach toward reconstructing the late-time near-horizon geometry of merging binary black holes, and toward computing gravitational-wave echoes from exotic compact objects. A binary black-hole merger spacetime can be divided by a timelike hypersurface into a black-hole perturbation (BHP) region (in which the spacetime geometry can be approximated by homogeneous linear perturbations of the final Kerr black hole) and a nonlinear region. At late times, the boundary between the two regions is an infalling shell. The BHP region contains late-time gravitational waves emitted toward the future horizon, as well as those emitted toward future null infinity. In this region, by imposing no-ingoing-wave conditions at past null infinity and matching outgoing waves at future null infinity with waveforms computed from numerical relativity, we can obtain waves that travel toward the future horizon. In particular, the Newman-Penrose $\psi_0$ associated with the ingoing wave on the horizon is related to tidal deformations measured by fiducial observers floating above the horizon. We further determine the boundary of the BHP region on the future horizon by imposing that $\psi_0$ inside the BHP region can be faithfully represented by quasinormal modes. Using a physically motivated method to impose boundary conditions near the horizon and applying the so-called Boltzmann reflectivity, we compute the quasinormal modes of nonrotating exotic compact objects, as well as gravitational-wave echoes. We also investigate the detectability of these echoes in current and future detectors and prospects for parameter estimation.

DOI: 10.1103/PhysRevD.105.104007

## I. INTRODUCTION

Delayed and repeating gravitational-wave echoes emitted by compact-binary mergers [1–3] following the main gravitational waves (GWs) can be signatures of (i) deviations of laws of gravity from general relativity [4,5], (ii) near-horizon quantum structures surrounding black holes (BHs) [6–15], and (iii) the absence of an event horizon—namely, the existence of horizonless exotic compact objects (ECOs) [16–20]. We emphasize that strong arguments (within the context of general relativity and the standard model of matter) exist against the existence of echoes and ECOs, including (i) the ergoregion instability [21–24], (ii) the formation of a trapped surface due to the pileup of energy near the stable photon orbit [25–28], (iii) the collapse of the ECO due to the gravity of incident GWs [29,30], and (iv) other nonlinear effects [31]. Nevertheless, if GW echoes do exist, their detection will serve as an important tool for studying the physics of BHs or ECOs. A lot of effort has been made to search for echoes in observed data (see Ref. [32] for a thorough review). As a result, constructing accurate waveform models for GW echoes is necessary and timely [33,34].

If we restrict deviation from general relativity (GR) to be localized near the would-be horizon, then, due to Birkhoff's theorem, the region outside a spherically symmetric ECO can still be described by a Schwarzschild geometry. Consequently, studies of echoes from nonspinning ECOs were based mostly on the black hole perturbation (BHP) theory and the Zerilli-Regge-Wheeler equations [35,36]. For instance, Cardoso and colleagues [1,2] showed that the initial ringdown signal of different ECO models has a universal feature and is identical to that of a Schwarzschild BH, even though the quasinormal mode (QNM) spectra of ECOs are completely different from the ones of the Schwarzschild BH. This implies that the initial pulse of the ringdown is more related to spacetime geometry near

*sma@caltech.edu
†yanbei@caltech.edu

 

the light ring than in the formal spectra of QNMs. The following echoes do depend on the structure of the QNM spectra [37], which is characterized by modes trapped between the ECO surface and the peak of the BH potential barrier [38]. Mark *et al.* [39] developed a framework to systematically compute scalar echoes from nonspinning ECOs (in terms of GWs propagating toward the would-be horizon) and transfer functions that convert this horizon-going wave into echoes toward infinity. Testa and Pani [40] used a Pöschl-Teller potential to approximate the BH potential for perturbations and derived an analytical echo template. Meanwhile, Du and Chen [41] estimated the contribution of GW echoes to the stochastic background. In terms of the membrane diagram, Maggio *et al.* [42] and Chakraborty *et al.* [13] treated the ECO surface as a dissipative fluid and related the reflectivity to the bulk and the shear viscosity. Cardoso *et al.* [43] studied the resonant excitation of the modes of nonspinning ECOs during an extreme-mass-ratio inspiral. More recently, the echoes of fuzz balls [44,45] were computed numerically in Ref. [46], and the GW echo from a three-body system was studied in Ref. [47].

In astrophysical situations, merger remnants usually have non-negligible spins [48]; hence, it is of great practical interest to model echoes from spinning ECOs. Even if GR is valid away from ECOs, the spacetime geometry there can deviate significantly from Kerr, as it has a general multipole structure [49,50]. Nevertheless, we shall restrict ourselves to the Kerr geometry, whose linear perturbation is described by the Teukolsky equation [51,52]. An early attempt at constructing echo waveforms studied scalar perturbations around a Kerr-like wormhole [53]. Working on a sourceless system, Nakano *et al.* [54] imposed a complete reflecting boundary condition at a constant Boyer-Lindquist radius. Later, the effect of source terms was investigated [55–60]. Sago and Tanaka [55] and Maggio *et al.* [56] studied main GWs and echoes generated by a particle that plunges into a Kerr black hole. The case of a particle (with scalar charge) sprialing into a Kerr black hole was studied in Ref. [57]. References [58–60] further introduced the backreaction of GW emissions on orbital motion.

Recently, Chen *et al.* [61] proposed a more physically motivated boundary condition by considering the tidal fields experienced by fiducial observers with zero angular momentum orbiting just above the ECO surface. This model established a relation between the ingoing component of the Weyl scalar $\psi_0$ and the outgoing piece of the Weyl scalar $\psi_4$. Using this new boundary condition, Xin *et al.* [59] calculated GW echoes by explicitly computing the $\psi_4$ falling down the ECO surface and converting it to $\psi_0$ via the Teukolsky-Starobinsky (TS) identity [62,63]. They found weaker echoes than those obtained using other approaches [10,64]. A flaw in their calculation is that the TS identity is applicable only in the absence of source terms. A direct computation of $\psi_0$ propagating toward the ECO surface was later carried out by Srivastava and Chen [60].

As we move away from extreme-mass-ratio inspirals, several approaches have been adopted to model echoes from comparable-mass binary black-hole (BBH) mergers. These include the *inside/outside* formulations, which do not involve modeling of the merger dynamics; the adaptation of the effective one-body (EOB) [65,66]; and the close-limit approximation (CLA) approaches [67–70]. All of these have played important roles in modeling BBH ringdown waveforms in GR.

In the *outside prescription* [71,72], the main GR GW emitted by a BBH merger was modeled as having been generated by the reflection of an initial pulse originating from null infinity (see Fig. 1 in Ref. [71]). The rest of this pulse travels through the light-ring potential and bounces back and forth between the surface of the ECO and the peak of the potential. As a result, a sequence of echoes follows the main GR GW at null infinity. In the *inside prescription* [10,64]. the main GR GW was modeled instead as the transmitted wave of an initial wave emerging from the past horizon (see Fig. 1 in Ref. [10]). Wang *et al.* [10] computed this initial wave by matching the main GW to that of a BBH merger event, whereas Maggio *et al.* [64] treated the main pulse as a superposition of QNMs, which led to analytical echo templates. Both the inside and outside prescriptions make direct connections between the main BBH GW and the ensuing echoes; they do not require detailed modeling of the merger dynamics.

In contrast, the approach based on the EOB formulation relies on the orbital dynamics. Following in the same spirit as the EOB method, Micchi *et al.* [58] considered the backreaction on the orbital evolution due to GW emissions. With a more accurate orbital dynamics, they were able to obtain a complete inspiral-merger-ringdown waveform and the subsequent echoes. Xin *et al.* [59] calibrated the dissipative force to a surrogate model [73,74] so that the GW at infinity matches the prediction of numerical relativity (NR).

Recently, the CLA approach was applied to computation of echoes from a head-on collision of two equal-mass ECOs [75], where the Brill-Lindquist initial data [76] for two BHs was ported into a linear perturbation of a single Schwarzschild spacetime, with a modified boundary condition on a surface right above the horizon.

In addition to the EOB and CLA approaches, a so-called hybrid approach [77,78] has also been proposed to jointly use post-Newtonian (PN) and BHP theories to model comparable-mass BBH mergers. To illustrate this method, a Penrose diagram of a BBH merger spacetime is shown in Fig. 1. The spacetime is split by a timelike world tube $\Sigma_{\text{Shell}}$ (which asymptotes toward a null tube in its upper-left section) into an inner PN region (III) and an outer BHP region (I + II). The hybrid approach offers a way to construct spacetime geometries in both regions—including

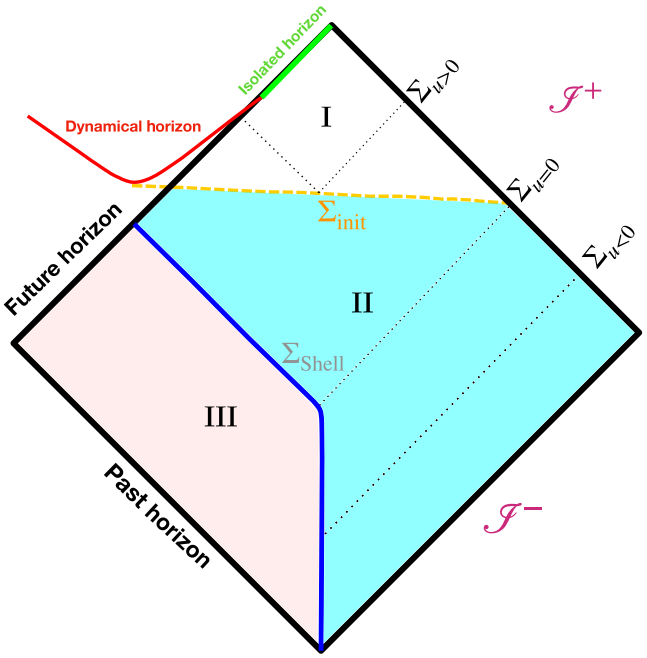


FIG. 1. Spacetime of a BBH merger event. The hybrid method divides the spacetime into an inner PN region (III) and an outer BHP region (I + II). The two regions communicate via boundary conditions at the world tube $\Sigma_{\rm Shell}$ (the blue curve), which was assumed to track the motion of the BH. The dynamical horizon (the red curve) lies inside the future horizon, and it eventually settles down to the isolated horizon. The common horizon forms at the time slice $\Sigma_{\rm init}$ (the horizontal dashed line). The time slice $\Sigma_{\rm init}$ is not unique and is determined by gauge conditions. The CLA focuses exclusively on region I, where the system is treated as a Cauchy problem—initial data need to be provided on $\Sigma_{\rm init}$, whereas the hybrid method gives attention to regions both I and II and handles the system as a boundary value problem.

GWs at null infinity; it was able to accurately predict the GW waveform and kick velocity of a head-on collision [77,78].

In this paper, we shall take a point of view similar to the hybrid approach—by dividing the spacetime into a linear BHP region (I and II in Fig. 1) and a region (III) in which the spacetime is not a linear perturbation of the remnant BH. We shall not attempt to *approximately solve for* the entire spacetime geometry in all regions, but instead use the gravitational waveform at the null infinity $\mathcal{I}^+$ already obtained from NR to reconstruct the spacetime geometry in the BHP region—including GWs propagating toward the future horizon $\mathcal{H}^+$. In particular, we find the location of the world tube $\Sigma_{\rm Shell}$ at $\mathcal{H}^+$ can be determined by looking for when the linearly quasinormal ringing of the horizon GW starts. Equipped with this information, together with the recent physically motivated boundary condition near the would-be future horizon [61], we can construct gravitational echoes at $\mathcal{I}^+$.

As a first step toward demonstrating our spacetime reconstruction approach, in this paper, we restrict ourselves to inspiraling BBHs whose remnants are nonrotating.[1] Specifically, we shall use a NR technique *Cauchy-characteristic extraction* (CCE) [79–84] to extract the Weyl scalars $\psi_4$ and $\psi_0$ of the BBH events in question and use them to reconstruct spacetime geometry in the linear BH regions I and II.

This paper is organized as follows. In Sec. II we explain spacetime reconstruction in more detail using Fig. 1 and outline the basic ideas of the hybrid method. We then describe our NR techniques and simulations in Sec. III. Taking these NR simulations, we explicitly carry out spacetime reconstruction in Sec. IV, in particular, by obtaining gravitational waves propagating toward the future horizon $\mathcal{H}^+$. With these horizon waveforms, we construct gravitational-wave echoes at $\mathcal{I}^+$ in Sec. V. Section VI focuses on the detectability of GW echo and parameter estimation, using the Fisher information matrix formalism. Finally, in Sec. VII we summarize our results.

Throughout this paper, we use the geometric units $G = c = 1$. Unless stated otherwise, we use the remnant mass $M_f$ to normalize all dimensional quantities[2] (e.g., time, length, and Weyl scalars). Note that this choice is different from the typical convention adopted by the NR community, where the initial total mass of the system $M_{\rm tot}$ is used.

## II. SPACETIME RECONSTRUCTION FROM GRAVITATIONAL WAVES AT FUTURE NULL INFINITY: THEORY

In this section, we shall describe our theoretical strategy for spacetime reconstruction based on BBH GWs at the future null infinity $\mathcal{I}^+$. We shall divide the entire spacetime into two regions, the black-hole perturbation region (I + II in Fig. 1) and the strong-field region (III in Fig. 1), as proposed during the construction of the hybrid model for BBH coalescence [77,78]. In Sec. II A, we shall review the hybrid method, focusing on how spacetime geometry in the bulk of the BHP region depends on boundary values. In Sec. II B, we discuss in particular how the bulk geometry can be expressed in terms of waves at $\mathcal{I}^+$. In Sec. II C, we focus on GWs that propagate toward the future horizon $\mathcal{H}^+$, proposing in particular a way to determine the boundary between the BHP region II and the strong field region III. In Sec. II D, we comment on how our approach is connected to previous works.

### A. From the hybrid method to spacetime reconstruction

In the Penrose diagram of a coalescing BBH spacetime (Fig. 1), the red curve represents the dynamical horizon,

[1]The initial parameters of BBHs are fine-tuned so that the remnants are Schwarzschild BHs. Our method will also be applicable to head-on collisions.

[2]Namely, $M_f = 1$.

which is well known to be inside the event horizon [85]. Nichols and Chen [77] proposed using a three-dimensional timelike tube $\Sigma_{\rm Shell}$, shown as a blue curve, to divide the spacetime into two regions. The exterior regions (I + II) can be treated as a linearly perturbed Schwarzschild spacetime. Interior to the tube $\Sigma_{\rm Shell}$ is a strong-field region (III) which Nichols and Chen modeled using post-Newtonian theory; this PN metric is matched to the exterior perturbed Schwarzschild metric on the $\Sigma_{\rm Shell}$. Note that the PN expansion for the interior spacetime may break down in the late stages of evolution, but the shell falls rapidly to the horizon, so the errors might stay within the BH potential and not propagate toward infinity.

For a head-on collision, the tube $\Sigma_{\rm Shell}$ passes through the centers of the two BHs and follows the geodesic plunge of the remnant BH (i.e., the BH on which regions I and II are based). A more sophisticated framework was developed later [78] to determine the motion of $\Sigma_{\rm Shell}$ for an inspiraling BBH system. This framework added a radiation-reaction force to account for the dissipative effect of the GW emission. In the end, this PN-BHP system, accompanied by the no-incoming-wave condition at $\mathcal{I}^-$, forms a complete set of evolution equations, which leads to an approximated, *ab initio* waveform model. This method was able to predict a reasonable waveform for a BBH system merging in quasicircular orbits.

In this paper, we focus mainly on the region I + II, where the spacetime is treated as a linear perturbation to a Schwarzschild BH. Let us first examine this linear perturbation using the Sasaki-Nakamura (SN) formalism [86], in which the SN variable ${}_s\Psi^{\rm SN}_{lm}$ satisfies the Regge-Wheeler (RW) equation [35]

$$\left(\frac{\partial^2}{\partial u\partial v}+\frac{V^l_{\rm RW}}{4}\right){}_s\Psi^{\rm SN}_{lm}=0, \tag{1}$$

where $u=t-r_*$ and $v=t+r_*$ are the retarded and advanced times, respectively, with the tortoise coordinate $r_*=r+2\ln(\frac{r}{2}-1)$. The RW potential reads [87]

$$V^l_{\rm RW}=\frac{\Delta}{r^5}[(l^2+l)r-2(s^2-1)]. \tag{2}$$

Here $s$ corresponds to the spin weight of ${}_s\Psi^{\rm SN}_{lm}$ and $\Delta=r^2-2r$. In the hybrid approach, no-incoming-wave condition was imposed on $\mathcal{I}^-$, while PN data was imposed on $\Sigma_{\rm shell}$. One way to obtain ${}_s\Psi^{\rm SN}_{lm}$ throughout regions I + II from these boundary conditions is to use the characteristic method that we discuss in Appendix B.

In this paper, while keeping the no-incoming condition on $\mathcal{I}^-$, we shall revert the rest of the reconstruction process by imposing outgoing waves obtained from NR on $\mathcal{I}^+$ (e.g., with the CCE method). In particular, we shall obtain perturbative fields near $\mathcal{H}^+$, which will inform us about the gravitational waveform going down the horizon and serve as a foundation for obtaining GW echoes.

### B. Spacetime reconstruction using homogeneous Teukolsky solutions

As we reconstruct spacetime geometry, instead of SN variables, we will directly consider both $\psi_0$ and $\psi_4$ because they have explicit physical meanings, as explained in Ref. [61]. Since the new boundary $\mathcal{I}^+\cup\mathcal{I}^-$ for spacetime reconstruction has a regular shape (unlike $\Sigma_{\rm shell}$), we can carry out spacetime reconstruction by superimposing homogeneous solutions to the Teukolsky equation that already satisfy the no-ingoing boundary condition—traditionally referred to as the *up solutions*.

Let us first write general homogeneous solutions for $\psi_0$ and $\psi_4$ in mode expansions:

$$\psi_4(t,r,\theta,\phi)=\frac{1}{r^4}\sum_{lm}\int d\omega\,{}_{-2}R_{lm\omega}(r)\,{}_{-2}Y_{lm}(\theta,\phi)e^{-i\omega t}, \tag{3a}$$

$$\psi_0(t,r,\theta,\phi)=\sum_{lm}\int d\omega\,{}_{+2}R_{lm\omega}(r)\,{}_{+2}Y_{lm}(\theta,\phi)e^{-i\omega t}. \tag{3b}$$

Here ${}_sY_{lm}$ are spin-weighted spherical harmonics. The radial functions ${}_sR_{lm\omega}(r)$ satisfy the radial Teukolsky equation [52]

$$\Delta^{-s}\frac{d}{dr}\left(\Delta^{s+1}\frac{d}{dr}{}_sR_{lm\omega}\right)+V\,{}_sR_{lm\omega}=0, \tag{4}$$

with

$$V=4is\omega r-l(l+1)+\frac{r^4\omega^2-2is(r-M)r^2\omega}{\Delta}.$$

The up solutions, with their conventional normalization (with unity outgoing wave amplitude at infinity), have the following asymptotic forms near infinity and horizon:

$${}_{-2}R^{\rm up}_{lm\omega}\sim\begin{cases} r^3e^{i\omega r_*}, & r_*\to+\infty,\\ D^{\rm out}_{lm\omega}e^{i\omega r_*}+\Delta^2D^{\rm in}_{lm\omega}e^{-i\omega r_*}, & r_*\to-\infty,\end{cases} \tag{5a}$$

$${}_{+2}R^{\rm up}_{lm\omega}\sim\begin{cases} r^{-5}e^{i\omega r_*}, & r_*\to+\infty,\\ C^{\rm out}_{lm\omega}e^{i\omega r_*}+\Delta^{-2}C^{\rm in}_{lm\omega}e^{-i\omega r_*}, & r_*\to-\infty.\end{cases} \tag{5b}$$

Numerical values of the coefficients $C^{\rm in/out}_{lm\omega}$ and $D^{\rm in/out}_{lm\omega}$ are available from the Black Hole Perturbation Toolkit [88].

In a BBH coalescence spacetime, the $\psi_0$ and $\psi_4$ in the I + II region have the following asymptotic forms:

$$ {}_{-2}R^{\rm BBH}_{lm\omega} \sim \begin{cases} r^3 Z^{\infty}_{lm\omega} e^{i\omega r_*}, & r_* \to +\infty, \\ Z^{\rm H\,out}_{lm\omega} e^{i\omega r_*} + \Delta^2 Z^{\rm H\,in}_{lm\omega} e^{-i\omega r_*}, & r_* \to -\infty, \end{cases} \tag{6a} $$

$$ {}_{+2}R^{\rm BBH}_{lm\omega} \sim \begin{cases} r^{-5} Y^{\infty}_{lm\omega} e^{i\omega r_*}, & r_* \to +\infty, \\ Y^{\rm H\,out}_{lm\omega} e^{i\omega r_*} + \Delta^{-2} Y^{\rm H\,in}_{lm\omega} e^{-i\omega r_*}, & r_* \to -\infty. \end{cases} \tag{6b} $$

Here the amplitudes at infinity, $Z^{\infty}_{lm\omega}$ and $Y^{\infty}_{lm\omega}$ in Eq. (6), can be directly obtained from NR simulations. For completeness, the strain $h^{\infty}_{lm}$ observed at $\mathcal{I}^+$ is related to $Z^{\infty}_{lm\omega}$ via

$$ h^{\infty}_{lm}(\omega) = \frac{1}{\omega^2} Z^{\infty}_{lm\omega}. \tag{7} $$

Note that $h^{\infty}_{lm}$ is defined later in Eq. (15b). By comparing Eqs. (6) with the standard up solutions in Eqs. (5), we can obtain amplitudes near the horizon:

$$ Z^{\rm H\,out}_{lm\omega} = D^{\rm out}_{lm\omega} Z^{\infty}_{lm\omega}, \qquad Z^{\rm H\,in}_{lm\omega} = D^{\rm in}_{lm\omega} Z^{\infty}_{lm\omega}, \tag{8a} $$

$$ Y^{\rm H\,out}_{lm\omega} = C^{\rm out}_{lm\omega} Y^{\infty}_{lm\omega}, \qquad Y^{\rm H\,in}_{lm\omega} = C^{\rm in}_{lm\omega} Y^{\infty}_{lm\omega}. \tag{8b} $$

In this way, from the waves escaping at infinity, $Z^{\infty}_{lm\omega}$ and $Y^{\infty}_{lm\omega}$, the coefficients $D^{\rm in}_{lm\omega}$ and $C^{\rm in}_{lm\omega}$ will allow us to reconstruct ingoing waves $Z^{\rm in}_{lm\omega}$ and $Y^{\rm in}_{lm\omega}$ toward $\mathcal{H}^+$. We plot $D^{\rm in}_{22\omega}$ and $C^{\rm in}_{22\omega}$ in Fig. 2.

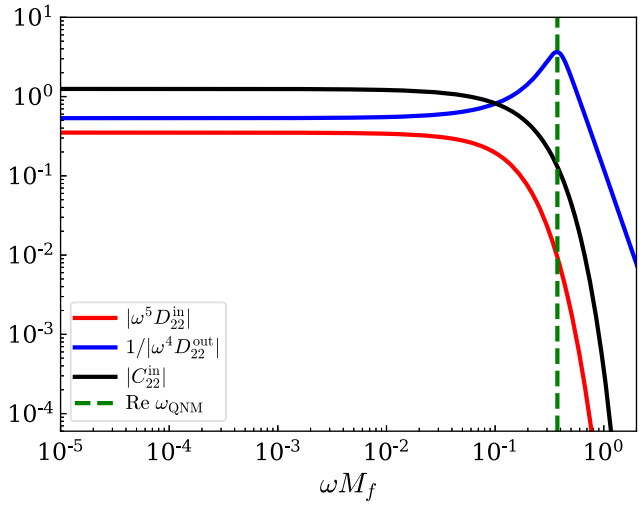


FIG. 2. Coefficients $C^{\rm in}_{lm\omega}$ and $D^{\rm in/out}_{lm\omega}$ predicted by the Teukolsky equation, assuming a Schwarzschild BH. The vertical dashed line stands for the real part of the fundamental QNM $(0.374 - 0.0890i)$. Data were obtained from the Black Hole Perturbation Toolkit [88].

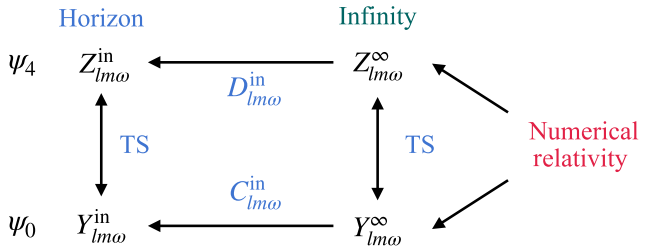


FIG. 3. Diagram summarizing the relations between BHP quantities on the horizon, $Z^{\rm in}_{lm\omega}$ and $Y^{\rm in}_{lm\omega}$, and those at infinity, $Z^{\infty}_{lm\omega}$ and $Y^{\infty}_{lm\omega}$.

We note that for the same linear perturbative spacetime of Schwarzschild governed by the vacuum Teukolsky equation, the $\psi_0$ and $\psi_4$ can be related by the TS relations, which state that [62,63]

$$ \frac{4\omega^4}{C^*} Y^{\infty}_{lm\omega} = Z^{\infty}_{lm\omega}, \tag{9a} $$

$$ Y^{\rm H\,in}_{lm\omega} = \frac{D}{C} Z^{\rm H\,in}_{lm\omega}, \tag{9b} $$

with

$$ C = (l-1)l(l+1)(l+2) + 12i\omega, \tag{10a} $$

$$ D = 64i\omega(128\omega^2 + 8)(1 - 2i\omega). \tag{10b} $$

These relations are consistent with the coefficients in Eqs. (8). For example, because[3]

$$ \frac{|C|^2}{4\omega^4} C^{\rm in}_{lm} = D D^{\rm in}_{lm}, \tag{11} $$

one can obtain $Y^{\rm H\,in}$ from $Z^{\infty}$ by either (i) using the TS relation at infinity to obtain $Y^{\infty}$, followed by Eq. (8b), or (ii) using Eq. (8a) to obtain $Z^{\rm H\,in}$, and then using the TS relation near the horizon [i.e., Eq. (9b)]. Relations between the BHP quantities have been summarized in Fig. 3. We shall check the TS relations directly in Sec. IV A.

We would like to caution here that, while it has been established [62,63] that the TS transformation maps between solutions of $\psi_0$ and $\psi_4$, these works alone did not explicitly establish the one-to-one relations in Eqs. (9) between $Z_{lm\omega}$ and $Y_{lm\omega}$ for the same GW. Further work by Wald [89] explicitly related both $\psi_0$ and $\psi_4$ to the Hertz potential, while more recent work by Loutrel *et al.* [90] provided a new way to reconstruct the metric (hence $\psi_0$) from $\psi_4$. From Ref. [90], for the same generic GW, the one-to-one relation is between $(Z_{l,m,\omega}, Z_{l,-m,-\omega})$ and

[3]We have checked to ensure that Eq. (11) holds up to numerical accuracy, which is of the order of $10^{-13}$ for the Black Hole Perturbation Toolkit.

$(Y_{l,m,\omega}, Y_{l,-m,-\omega})$ rather than simply between $Z_{lm\omega}$ and $Y_{lm\omega}$. Nevertheless, as will be seen later in this paper (see Sec. IV A), our numerical results for $\psi_0$ and $\psi_4$ agree with Eqs. (9). This might be due to the fact that we have nonprecessing systems which satisfy [91]

$$Z_{l,m,\omega} = (-1)^l Z^*_{l,-m,-\omega}, \qquad Y_{l,m,\omega} = (-1)^l Y^*_{l,-m,-\omega}. \quad (12)$$

However, for more generic (e.g., precessing) binaries, the naive TS relation Eqs. (9) may not hold.

### C. Connection to the inside prescription and determination of the location of $\Sigma_{\rm Shell}$

To understand the physical meaning of $Z^{\rm H\,out}_{lm\omega}$ and $Y^{\rm H\,out}_{lm\omega}$, which mathematically appears to be emitted from the past horizon $\mathcal{H}^-$, we have to go to Fig. 4 and remind ourselves that region I + II does not contain the past horizon of the background BH. Anything below the red curve (the shell)

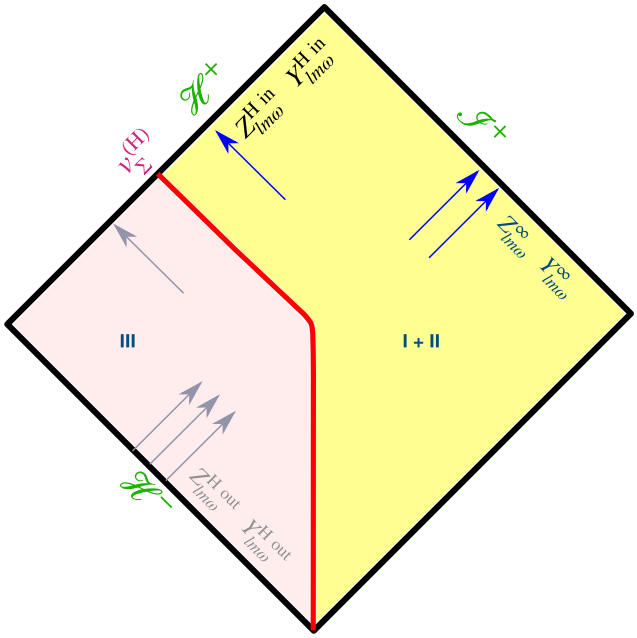


FIG. 4. Spacetime diagram illustrating the BHP region I + II and its linear extrapolation into region III. Outside the matching shell, curvature perturbations are linear combinations of the up-mode solutions to the homogeneous Teukolsky equation. At infinity $\mathcal{I}^+$, the values of $Z^{\infty}_{lm\omega}$ and $Y^{\infty}_{lm\omega}$ are chosen to be consistent with the predictions of CCE. The past horizon exists in the strong gravity region III, where $Z^{\rm H\,out}_{lm\omega}$ and $Y^{\rm H\,out}_{lm\omega}$ represent the image wave that gives rise to waves in the region I + II. They serve the same role as the initial wave packet within the inside prescription [10,64]. The future horizon lies partially outside the matching shell: only the outside portion $(v > v_\Sigma^{\rm (H)})$ of $Z^{\rm H\,in}_{lm}$ and $Y^{\rm H\,in}_{lm}$ corresponds to the actual wave that falls down the horizon. One natural way to self-consistently determine the location of $\Sigma_{\rm shell}$ is to evaluate the starting time after which $Y^{\rm H\,in}_{lm}(v)$ can be decomposed as a sum of QNM overtones. More details can be found in Sec. IV B.

in Fig. 4 are *linear extrapolations*. Nevertheless, this extrapolation asserts that waveforms at infinity can be thought of as being generated by "image waves" with $Z^{\rm H\,out}$ and $Y^{\rm H\,out}$ that rise from the past horizon. This follows the same reasoning as the inside prescription [10,64].

Since the image wave encounters the BH potential barrier (from the inside), it is partially transmitted toward $\mathcal{I}^+$ while partially reflected toward $\mathcal{H}^+$. We can rewrite

$$Z^{\infty}_{lm\omega} = \frac{1}{D^{\rm out}_{lm\omega}} Z^{\rm H\,out}_{lm\omega}, \qquad Z^{\rm H\,in}_{lm\omega} = \frac{D^{\rm in}_{lm\omega}}{D^{\rm out}_{lm\omega}} Z^{\rm H\,out}_{lm\omega}, \quad (13a)$$

$$Y^{\infty}_{lm\omega} = \frac{1}{C^{\rm out}_{lm\omega}} Y^{\rm H\,out}_{lm\omega}, \qquad Y^{\rm H\,in}_{lm\omega} = \frac{C^{\rm in}_{lm\omega}}{C^{\rm out}_{lm\omega}} Y^{\rm H\,out}_{lm\omega}. \quad (13b)$$

Here $1/D^{\rm out}_{lm\omega}$ and $1/C^{\rm out}_{lm\omega}$ are the transmissivities from $\mathcal{H}^-$ to $\mathcal{I}^+$ across the potential barrier, while $D^{\rm in}_{lm\omega}/D^{\rm out}_{lm\omega}$ and $C^{\rm in}_{lm\omega}/C^{\rm out}_{lm\omega}$ are reflectivities at the potential barrier that direct the wave toward $\mathcal{H}^+$. (The dependence of $1/D^{\rm out}_{22\omega}$ on $\omega$ is plotted in Fig. 2.)

In this way, we have shown that the inside prescription and the hybrid method correspond to the same reconstruction of spacetime geometry in the regime where the linear BHP applies. However, we want to emphasize that the two methods adopt different approaches when choosing the linear BHP region. In the hybrid method, it is given by the exterior region of $\Sigma_{\rm Shell}$. In particular, in order to compute echoes, we shall need to terminate the linear perturbation region at the intersection of the shell $\Sigma_{\rm shell}$ and the future horizon, which is denoted by the advanced time $v = v_\Sigma^{\rm (H)}$ in Fig. 4. One natural way to determine the intersection is to first evaluate the time-domain waveform

$$Y^{\rm H\,in}_{lm}(v) = \int d\omega Y^{\rm H\,in}_{lm\omega} e^{-i\omega v} \quad (14)$$

and then define $v_\Sigma^{\rm (H)}$ as the starting time after which $Y^{\rm H\,in}_{lm}(v)$ can be decomposed as a sum of the QNM overtones. We shall provide more details when we carry out this decomposition in Sec. IV B.

On the contrary, the inside prescription uses only the late-time evolution as the linear region. We shall have more discussions regarding this comparison in Sec. II D.

### D. Further comparisons with the inside prescription and the close-limit approximation

To fit the inside prescription into our framework, in Fig. 1, we choose a time slice $\Sigma_{\rm init}$ after which the spacetime (i.e., region I) is consistent with that of a single perturbed BH. The time slice is usually not unique and is determined by a gauge condition. An appropriate choice is to let $\Sigma_{\rm init}$ represent a moment when the common horizon just forms, following the close-limit approximation [92–99]. Then the inside prescription corresponds to taking

only region I and treating it as the linear BHP area. Consequently, one needs to take the ringdown of the main GWs at the null infinity as input, which is equivalent to imposing a filter at $\mathcal{I}^+$ [64], and use that information to calculate the echoes. In fact, since region II is not included, the indeterminate condition at past null infinity leaves room for the outside prescription [71,72].

Similarly, the CLA corresponds to region I as well. This is an approach to studying the spacetime based on the fact that the gravitational field in region I can be modeled as that of a single perturbed BH. The system in region I is then treated as a Cauchy problem (i.e., an initial value problem) as long as initial data are provided on $\Sigma_{\rm init}$. Previous studies have investigated the Misner initial data [100], the Brill-Lindquist initial data [76], the Bowen-York initial data [101], and numerically generated initial data [102,103]. Once the gravitational field in region I is solved, one can read off the value of $Z^{\rm H\,in}_{lm\omega}$ and $Y^{\rm H\,in}_{lm\omega}$ at the future horizon and compute echo waveforms [75].

The hybrid method, however, is a boundary value problem. It divides the spacetime into two regions via the timelike shell $\Sigma_{\rm Shell}$, as opposed to the spacelike hypersurface $\Sigma_{\rm init}$ adopted by the CLA. In addition, regions I and II are both regarded as BHP areas.

## III. NUMERICAL-RELATIVITY SIMULATIONS

In this section, we adopt two BBH merger simulations performed using the Spectral Einstein Code (SpEC) [104] developed by the Simulating eXtreme Spacetimes (SXS) collaboration [105]. These binaries have their initial parameters fine-tuned such that the remnant black holes are nearly nonspinning. Gravitational waveforms (at infinity) of these simulations are publicly available through the SXS catalog [105] with the identifiers SXS:BBH:0207 and SXS:BBH:1936.

We summarize the properties of these binaries in Table I, where we adopt the standard convention in SpEC, namely, by labeling the heavier hole with "1" and the lighter one with "2" and assuming the $z$ axis to be aligned with the initial orbital angular momentum. Our two systems have mass ratios $q = m_2/m_1 = 7, 4$, respectively; they undergo $N_{\rm cycle} = 36, 16.5$ orbit cycles before the merger, with the initial orbital eccentricity already reduced to $\sim 10^{-4}$. Both systems are nonprecessing, with initial spins antialigned with the orbital angular momentum (or vanishing), as indicated by the negative signs of the dimensionless spin components, $\chi^z_1$ and $\chi^z_2$. The remnant BHs have small spins at the $\chi_f \sim 10^{-2}$ level, with the remnant mass $M_f$ slightly less than the initial total mass of the system $M_{\rm tot} = m_1 + m_2$.

We extract gravitational waveforms at the null infinity $\mathcal{I}^+$ using the CCE method [83,84] implemented in the new NR code SpECTRE [106,107]. The CCE system evolves the Einstein field equations on a foliation of null hypersurfaces, where the metric is written in the Bondi-Sachs coordinates [108]. This method is most efficient in evolving the spacetime far from the BBH system and is reliable enough to produce all Weyl scalars $\psi_{0,1,2,3,4}$ with high accuracy [83,84]. In practice, CCE first reads off boundary data on a world tube covered by the inner Cauchy evolution, and then evolves a hierarchical system from the world tube toward future null infinity. The radii of the extraction world tubes for SXS:BBH:0207 and SXS:BBH:1936 are summarized in Table I. As in the standard treatment in NR, CCE decomposes each of the Weyl scalars $\psi_{0,1,2,3,4}$ and the strain $h$ into sums over a set of spin-weighted spherical harmonics ${}_sY_{lm}(\theta,\phi)$. Using the notation defined in Eqs. (6), the decomposition reads

$$[rM_f\psi_4]_{\mathcal{I}^+} = \sum_{l,m} {}_{-2}Y_{lm}(\theta,\phi) Z^{\infty}_{lm}, \tag{15a}$$

$$[rh/M_f]_{\mathcal{I}^+} = \sum_{l,m} {}_{-2}Y_{lm}(\theta,\phi) h^{\infty}_{lm}, \tag{15b}$$

$$[r^5 M_f^{-3}\psi_0]_{\mathcal{I}^+} = \sum_{l,m} {}_{+2}Y_{lm}(\theta,\phi) Y^{\infty}_{lm}, \tag{15c}$$

where $\theta$ and $\phi$ are the polar and azimuthal angles, respectively, on the sky in the source frame. Note that in Eqs. (15) the asymptotic $r$ dependences of $\psi_4$, $h$, and $\psi_0$, as $r \to \infty$, are consistent with the peeling theorem [109]. Furthermore, these fields are normalized by the appropriate powers of $M_f$ such that $Z^{\infty}_{lm}$, $Y^{\infty}_{lm}$, and $h^{\infty}_{lm}$ are dimensionless. We want to emphasize again that, as opposed to the

TABLE I. Summary of NR simulations used in this paper. The first column is the identifier in the SXS catalog [105]. In the second column, $q = m_2/m_1 > 1$ shows the mass ratio. The third column is the number of orbit cycles that a system undergoes before the merger. The fourth and fifth columns give the initial individual dimensionless spins. They have only a $z$ component, where the $z$ axis is chosen to be aligned with the orbital angular momentum. The sixth and seventh columns exhibit the remnant mass (in the unit of initial total mass $M_{\rm tot}$) and remnant spin. The final column corresponds to the radius of the extraction world tube for CCE.

| ID SXS:BBH | $q$ | $N_{\rm cycle}$ | $\chi^z_1$ | $\chi^z_2$ | $\frac{M_f}{M_{\rm tot}}$ | $\chi_f$ | Extraction radius ($M_{\rm tot}$) |
|---|---|---|---|---|---|---|---|
| 0207 | 7.0 | 36 | −0.6 | $10^{-6}$ | 0.991 | −0.077 | 300 |
| 1936 | 4.0 | 16.5 | −0.8 | −0.8 | 0.985 | 0.022 | 273 |

usual NR convention, where the initial total mass of the system $M_{\rm tot}$ is used as the unit for time and length, in this paper, we use the remnant mass $M_f$ to normalize all dimensional quantities because we deal mainly with perturbations of the remnant (approximately) Schwarzschild BH.

Furthermore, we shift all temporal coordinates such that $u = 0$ corresponds to the peak of the total rms strain amplitude:

$$\sqrt{\sum_{lm}|h_{lm}(u)|^2}\Big|_{u=0} = \text{peak}. \tag{16}$$

## IV. NUMERICAL IMPLEMENTATIONS OF THE HYBRID METHOD

In this section, we apply the spacetime reconstruction procedure of Sec. II to SXS:BBH:0207 and SXS:BBH:1936. In Sec. IV A, we first investigate the validity of TS identities at the future null infinity $\mathcal{I}^+$ [see Eq. (9a)], given that the future null infinity lies completely in the BHP region. We also provide the horizon $\psi_0$ at the future horizon $\mathcal{H}^+$. Then in Sec. IV B, we use the horizon $\psi_0$ to determine the location of the matching tube $\Sigma_{\rm Shell}$ by looking for when its linearly quasinormal ringing starts.

### A. At null infinity and future horizon: The Weyl scalars and the Teukolsky-Starobinsky identities

For SXS:BBH:0207, we plot its $Z^{\infty}_{l=2,m=2}$ and $Y^{\infty}_{l=2,m=2}$ in Fig. 5 in both the time domain (upper panel) and the frequency domain (lower panel). In the frequency domain, $Z^{\infty}_{22}$ (black curve) peaks at the fundamental (2,2) quasinormal mode frequency (the vertical dotted line). On the other hand, $Y^{\infty}_{22}$ rises up sharply at low frequencies, where its magnitude is much greater than that of $Z^{\infty}_{22}$. This feature in the frequency domain is consistent with the TS identity at infinity [see Eq. (9a)]. To be concrete, we test the validity of Eq. (9a) in Fig. 6. The actual $Z^{\infty}_{22}$ (in black) is compared to $\frac{4\omega^4}{C^*}Y^{\infty}_{22}$ (in red) in the time domain (the left and center panels) and the frequency domain (the right panel). We see that the TS identity holds throughout the entire region. The comparison for SXS:BBH:1936 is similar and can be found in Appendix C.

At the future horizon, $Y^{\rm H\,in}_{lm}$ [Eq. (6)] is essential for us to compute echoes (see Sec. V A for more details). In Fig. 7, we plot $Y^{\rm H\,in}_{22}$ of SXS:BBH:0207 in the time domain (blue curve), where the advanced time $v$ is used as the time coordinate. Like $Y^{\infty}_{22}$ [see Fig. 5], $Y^{\rm H\,in}_{22}$ has a dominated low-frequency content. At early stage, $Y^{\rm H\,in}_{22}$ is inside the strong gravity region III and should be excised—as we shall discuss in Secs. IV B and V C. For comparison, we also plot $Y^{\infty}_{22}$ in the same figure (red curve)—using $u$ as the time coordinate. We caution that this comparison has only a qualitative meaning because the two waveforms are emitted in different directions. Showing the $v$ dependence of $Y^{\rm H\,in}_{22}$ and the $u$ dependence of $Y^{\infty}_{22}$ in the same plot effectively traces both of these waves back to the same time $t$ at $r_* = 0$. This is qualitatively meaningful because the ringdown wave can be thought of as having originated from the light ring at $r = 3M$, where $r_* \approx 0$. From this comparison, we can see that $Y^{\rm H\,in}_{22}$ decreases faster and undergoes fewer cycles of oscillation at the late phase than $Y^{\infty}_{22}$.

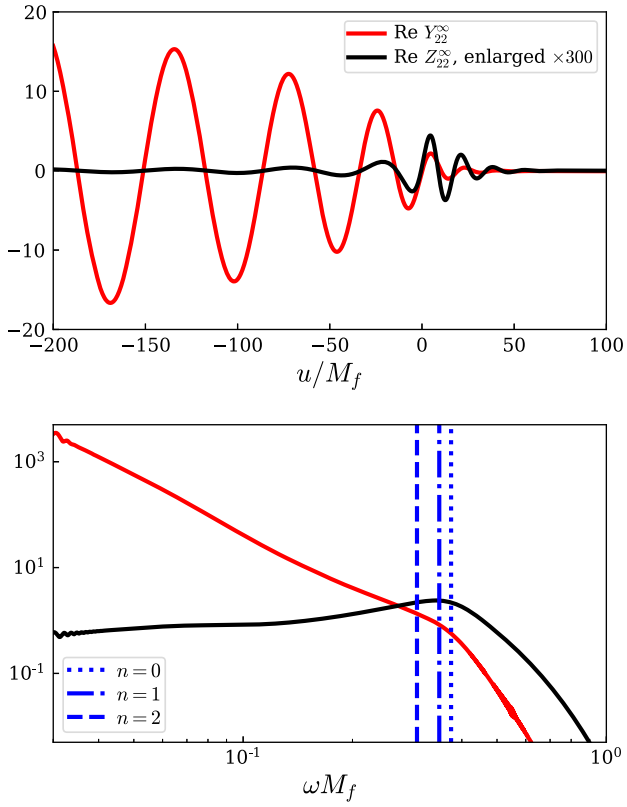


FIG. 5. Spherical modes $Y^{\infty}_{22}$ and $Z^{\infty}_{22}$ of SXS:BBH:0207 in the time domain (upper panel) and in the frequency domain (lower panel). The vertical lines in the lower panel represent QNM frequencies of a Schwarzschild BH, labeled with the overtone index $n$. The absolute value of $Z^{\infty}_{22}$ is amplified by a factor of 300 for simplicity.

### B. Determining the location of $\Sigma_{\rm Shell}$

As mentioned in Sec. II, the region outside the matching tube $\Sigma_{\rm Shell}$ is consistent with a sourceless, linearly perturbed Schwarzschild spacetime. Accordingly, the part of $Y^{\rm H\,in}_{lm}$ that is in region I + II can be decomposed into a sum of QNMs (in the time domain). Conversely, we can use this fact to determine the location of $\Sigma_{\rm Shell}$. Indeed, this method has been used not only to determine the start time of a BBH ringdown at the future infinity[4] [110] but also to investigate the dynamics of a final apparent horizon in a BBH system approaching to equilibrium [111]. More specifically, we write [112]

[4]The linear perturbation regime was found to be valid as early as the peak of strain if seven overtones were included.

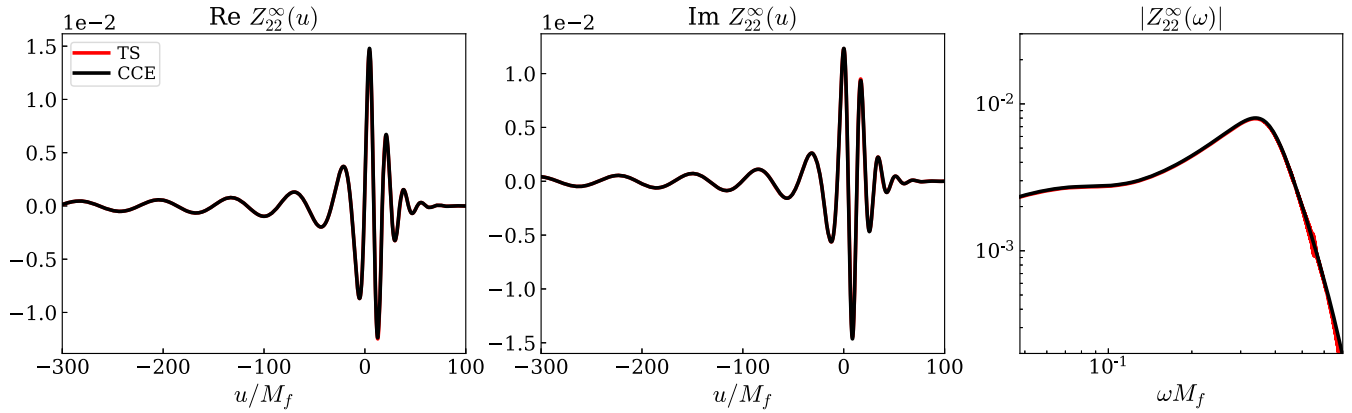


FIG. 6. Validity of the TS identity at infinity [Eq. (9a)] using SXS:BBH:0207. The predicted form $\frac{4\omega^4}{C^*}Y^{\infty}_{22}$ (in red) is compared to the actual $Z^{\infty}_{22}$ (in black) in the time domain (the left and center panels) and the frequency domain (the right panel). The comparison for SXS:BBH:1936 is in Fig. 20.

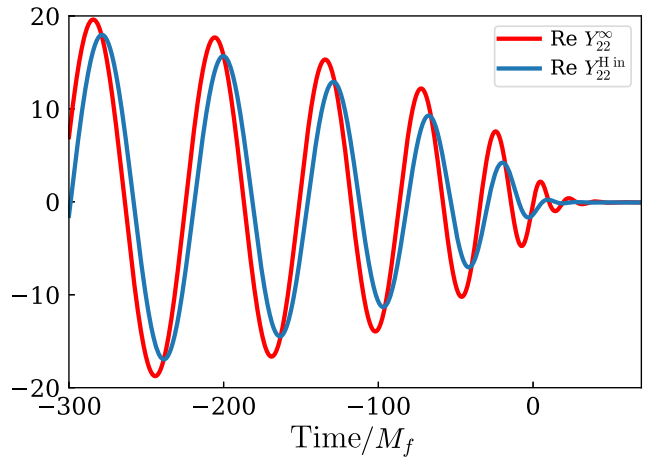


FIG. 7. Real part of $Y^{\mathrm{H\,in}}_{22}$ [Eqs. (6)] and $Y^{\infty}_{22}$ in the time domain using SXS:BBH:0207. The temporal coordinate for $Y^{\mathrm{H\,in}}_{22}$ is $v$, while is $u$ for $Y^{\infty}_{22}$. Both coordinates are in the unit of final mass.

$$h^{\infty}_{22}(u > u^{(h)}) = \sum_{n=0}^{n_{\max}} [\mathcal{A}^{(h)}_n e^{-i\omega_n u} + \mathcal{B}^{(h)}_n e^{i\omega^*_n u}], \tag{17a}$$

$$Y^{\infty}_{22}(u > u^{(\infty)}) = \sum_{n=0}^{n_{\max}} [\mathcal{A}^{(\infty)}_n e^{-i\omega_n u} + \mathcal{B}^{(\infty)}_n e^{i\omega^*_n u}], \tag{17b}$$

$$Y^{\mathrm{H\,in}}_{22}(v > v^{(\mathrm{H})}_{\Sigma}) = \sum_{n=0}^{n_{\max}} [\mathcal{A}^{(\mathrm{H})}_n e^{-i\omega_n v} + \mathcal{B}^{(\mathrm{H})}_n e^{i\omega^*_n v}], \tag{17c}$$

where $\omega_n$ is the QNM frequency of a Schwarzchild BH and $n$ refers to the overtone index (we have restricted it to $l = 2$). Note that for a Schwarzchild BH, the QNM frequency is independent of its spin weight and azimuthal quantum number. Unlike Giesler *et al.* [110], we include both prograde modes $\mathcal{A}_n$ and retrograde modes $\mathcal{B}_n$ for generality [113]. In Eqs. (17) we use $u^{(\infty/h)}$ and $v^{(\mathrm{H})}_{\Sigma}$ to indicate the time at which ringdown begins, and we emphasize again that the retarded time $u$ is used for $h^{\infty}_{22}$ and $Y^{\infty}_{22}$ at null infinity, whereas the advanced time $v$ is used for $Y^{\mathrm{H\,in}}_{22}$ at the future horizon.

In making the decomposition, we follow the procedure of Ref. [110]—namely, we use the mismatch $\mathcal{M}$ between the quasinormal mode ringdown waveform model (e.g., $h^{\mathrm{Ringdown}}_{22}$) and the NR result (e.g., $h^{\mathrm{NR}}_{22}$) as a loss function

$$\mathcal{M} = 1 - \frac{(h^{\mathrm{NR}}_{22}, h^{\mathrm{Ringdown}}_{22})}{\sqrt{(h^{\mathrm{Ringdown}}_{22}, h^{\mathrm{Ringdown}}_{22})(h^{\mathrm{NR}}_{22}, h^{\mathrm{NR}}_{22})}}, \tag{18}$$

with

$$(h^{\mathrm{NR}}_{22}, h^{\mathrm{Ringdown}}_{22}) = \mathrm{Re}\int_{u^{(h)}_{\Sigma}}^{T} h^{\mathrm{NR}}_{22} h^{\mathrm{Ringdown}*}_{22}\, dt, \tag{19}$$

where the upper limit of the integral $T$ is taken to be $90M_f$ after the peak of the total rms strain amplitude. In addition, we use unweighted linear least squares to fit the mode amplitudes and use nonlinear least squares to fit the final spin and mass. The mode frequency $\omega_n$ is obtained from the PYTHON package QNM [114]. During the fit, we find that the numerical accuracy of $Y^{\infty}_{22}$ and $Y^{\mathrm{H\,in}}_{22}$ is much worse than that of $h^{\infty}_{22}$, which makes the remnant mass and spin more difficult to recover.

In Fig. 8, we plot the mismatch $\mathcal{M}$ for $h^{\infty}_{22}$ (left panels), $Y^{\infty}_{22}$ (middle panels), and $Y^{\mathrm{H\,in}}_{22}$ (right panels) for SXS:BBH:0207 (upper panels) and SXS:BBH:1936 (lower panels). We see that the strain $h^{\infty}_{22}$ can be decomposed into the sum of the fundamental mode and six overtones.[5] For SXS:BBH:0207, the linear regime can be extended to $16M_f$ before the peak of $h^{\infty}_{22}$, whereas for SXS:BBH:1936

[5]Including more overtones no longer improves the match.

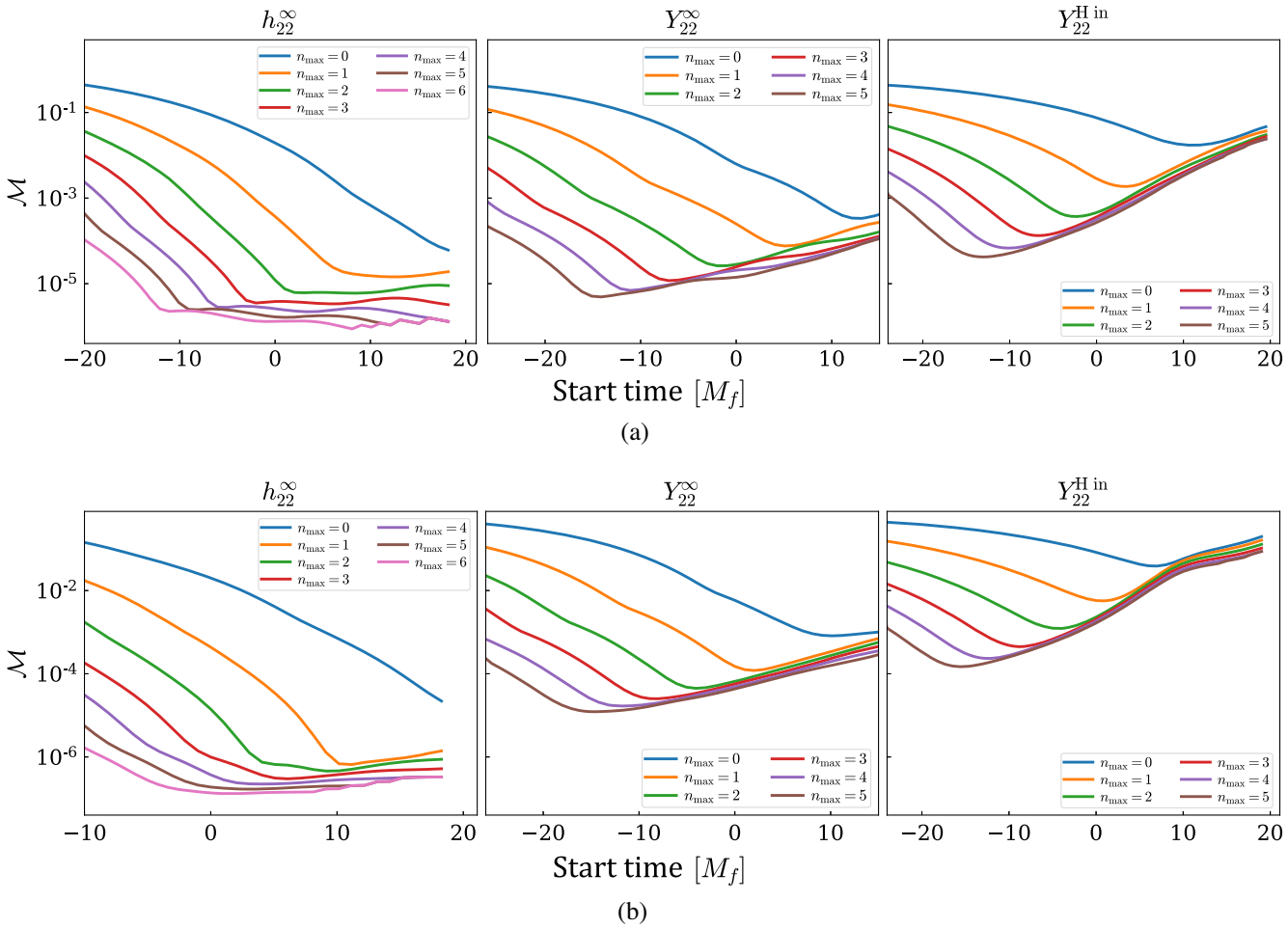


FIG. 8. Mismatch as a function of start time (in the unit of remnant mass) for different models [Eqs. (17)]. Each model includes up to $n_{\max}$ overtones. The left panels correspond to the strain $h_{22}^{\infty}$ at infinity, the middle panels correspond to $Y_{22}^{\infty}$, and the right panels correspond to $Y_{22}^{\mathrm{H\,in}}$ [see Eqs. (6) and (15b)]. (a) refers to SXS:BBH:0207, whereas (b) refers to SXS:BBH:1936. All waveforms are aligned such that $t = 0$ occurs at the peak of $\sqrt{\sum_{lm} |h_{lm}(t)|^2}$.

the linear quasinormal ringing regime starts from $2.0M_f$, similar to the case of GW150914 [110] and superkick systems [115].

On the other hand, since the numerical accuracy of $Y_{22}^{\infty}$ and $Y_{22}^{\mathrm{H\,in}}$ from CCE is not as high as $h_{22}^{\infty}$, only five overtones can be resolved. In particular, the late-time portion is dominated by numerical noise; therefore, the mismatch $\mathcal{M}$ tends to increase significantly. The start times of the linear regime for $h_{22}^{\infty}$, $Y_{22}^{\infty}$, and $Y_{22}^{\mathrm{H\,in}}$ are summarized in Table II. Below, we shall use the start time of $Y_{22}^{\mathrm{H\,in}}$, denoted by $v_{\Sigma}^{(\mathrm{H})}$, as the advanced time of the matching tube $\Sigma_{\mathrm{Shell}}$ (Figs. 1 and 4) and shall utilize the exterior portion of the GW to approximate the actual wave falling down the future horizon.

In addition to searching for the start time of the quasinormal ringing regime of $Y_{22}^{\mathrm{H\,in}}$, it is also interesting to investigate their QNM amplitudes [115,116]. This topic is beyond the scope of our study, but we provide a brief discussion of it in Appendix A.

TABLE II. Summary of the QNM decompositions of $h_{22}^{\infty}$, $Y_{22}^{\infty}$, and $Y_{22}^{\mathrm{H\,in}}$. The second row refers to the maximum number of overtones that we have included in Eq. (17). The third and fourth rows correspond to the time from which the waveform is consistent with a linear quasinormal ringing. The values are from the minimum of the corresponding curves in Fig. 8.

| | | $h_{22}^{\infty}$ | $Y_{22}^{\infty}$ | $Y_{22}^{\mathrm{H\,in}}$ |
|---|---|---|---|---|
| $n_{\max}$ | | 6 | 5 | 5 |
| $u^{(\infty/h)}$ or $v_{\Sigma}^{(\mathrm{H})}$ | SXS:BBH:0207 | −11.1 | −14.1 | −13 |
| | SXS:BBH:1936 | 2.0 | −14.2 | −15 |

## V. CONSTRUCTING ECHOES

Now we utilize the horizon-going GW obtained above to construct GW echoes at infinity. In Sec. V A, we first introduce physical boundary conditions near an ECO

surface [61] and obtain formulas that relate horizon waves to echoes at infinity. Then, in Sec. V B, we focus on the Boltzmann reflectivity and discuss QNM structures of the ECO. Next in Sec. V C, we compute echo waveforms numerically and investigate the impact of prescriptions made at the matching shell $\Sigma_{\rm Shell}$ (see Fig. 1), taking SXS:BBH:0207 as an example. Finally, we compare the hybrid method with the inside prescription in Sec. V D.

### A. Constructing echoes using the physical boundary condition near an ECO surface

Chen *et al.* [61] recently proposed imposing boundary conditions near the ECO surface using the membrane paradigm, in which a family of zero-angular-momentum fiducial observers (FIDOs) are considered. Within their own rest frame, the FIDOs experience a tidal tensor field [117]

$$\mathcal{E}_{ij} = h_i^a h_j^c C_{abcd} U^b U^d, \tag{20}$$

where $C_{abcd}$ is the Weyl tensor, $U^b$ is the four-velocity of the FIDOs, and $h_i^a = \delta_i^a + U^a U_i$ is the projection operator. The transverse component of $\mathcal{E}_{ij}$ [61],

$$\mathcal{E}_{\rm transverse} \sim -\frac{\Delta}{4r^2}\psi_0 - \frac{r^2}{\Delta}\psi_4^*, \tag{21}$$

is of particular interest since it represents the stretching and squeezing effect due to GW. In analogous to the tidal response of a neutron star, the response of the ECO was proposed to be linear in $\mathcal{E}_{\rm transverse}$; namely [61],

$$\left[-\frac{r^2}{\Delta}\psi_4^*\right]_{\rm surface} = \left[\frac{\mathscr{R}^{\rm ECO}}{\mathscr{R}^{\rm ECO}-1}\mathcal{E}_{\rm transverse}\right]_{\rm surface}. \tag{22}$$

The reflectivity $\mathcal{R}^{\rm ECO}$ depends on the (non-GR) property of ECO, as we shall discuss in Sec. V B.

Near the ECO surface, $\psi_0$ is dominated by the incident wave (toward the horizon), whereas $\psi_4$ by the reflected wave (by the ECO), i.e.,

$${}_{+2}R^{\rm ECO}_{lm}(u,v) \sim \int \frac{d\omega}{\Delta^2} Y^{\rm H\,in\,ECO}_{lm\omega} e^{-i\omega v}, \tag{23a}$$

$${}_{-2}R^{\rm ECO}_{lm\omega}(u,v) \sim \int d\omega Z^{\rm H\,out\,ECO}_{lm\omega} e^{-i\omega u}, \tag{23b}$$

with ${}_{\pm2}R^{\rm ECO}_{lm}(u,v)$ the radial Teukolsky function for the ECO. Here we use the same notation as Eqs. (6), and we emphasize that $Y^{\rm H\,in\,ECO}_{lm\omega}$ stands for the *actual* $\psi_0$ wave that falls down the future horizon.

After simplification, the boundary condition in Eq. (22) becomes

$$Z^{\rm H\,out\,ECO}_{lm\omega} = \frac{(-1)^{l+m+1}}{4}\mathscr{R}^{\rm ECO} Y^{\rm H\,in\,ECO}_{lm\omega}, \tag{24}$$

where we have used the following symmetry of a nonprecessing BBH system under reflection across the orbital plane [91]:

$$[Y^{\rm H\,in\,ECO}_{l,-m,-\omega}]^* = (-1)^l Y^{\rm H\,in\,ECO}_{lm\omega}. \tag{25}$$

Subsequently, the echo waveform at null infinity reads [59]

$$Z^{\infty{\rm echo}}_{lm\omega} = \mathcal{K}(\omega) Y^{\rm H\,in\,ECO}_{lm\omega}, \tag{26}$$

with the transfer function $\mathcal{K}(\omega)$,

$$\mathcal{K}(\omega) = \frac{(-1)^{l+m+1}\mathscr{R}^{\rm ECO}}{1-\mathscr{R}^{\rm ECO}\mathcal{R}^{\rm BHT}}\frac{1}{4D^{\rm out}_{lm}} = \frac{C}{DD^{\rm in}_{lm}}\sum_{n=1}(\mathscr{R}^{\rm ECO}\mathcal{R}^{\rm BHT})^n, \tag{27}$$

and

$$\mathcal{R}^{\rm BHT} = (-1)^{l+m+1}\frac{D^{\rm in}_{lm}}{D^{\rm out}_{lm}}\frac{D}{4C}. \tag{28}$$

In Eq. (27), we have written the total echo signal as a sum of individual echoes.

### B. The Boltzmann reflectivity

To model quantum effects around the horizon, Oshita *et al.* [11] and Wang *et al.* [10] proposed that GWs around the horizon interact with a quantum thermal bath. Specifically, these waves are subject to a position-dependent dissipation $\Omega(r_*)/E_{\rm Pl}$ and driven by a position-dependent stochastic source $\xi(r_*)$; levels of the driving and the dissipation are related using the fluctuation-dissipation theorem [118]. Then the BHP equation is modified as [10,11]

$$\left[-i\gamma\frac{\Omega(r_*)}{E_{\rm Pl}}\frac{d^2}{dr_*^2} + \frac{d^2}{dr_*^2} + \omega^2 - V^l_{\rm RWZ}\right]{}_s\Psi^{\rm SN}_{lm}(r_*) = \xi(r_*), \tag{29}$$

where $\Omega(r_*) = |\omega|/\sqrt{|g_{00}(r_*)|}$ is the proper frequency measured in the frame of the Schwarzschild observers, $E_{\rm Pl}$ is the Planck energy, and $\gamma$ is a dimensionless dissipation parameter that controls how the damping ramps up as the wave gets close to the horizon. Note that Eq. (29) reduces to the classical Zerilli-RW equation in the limit of $\gamma \to 0$ (vanishing of the dissipative effect) and $\xi \to 0$ (vanishing of the fluctuation source). Consequently, the modified equation leads to the following Boltzmann reflectivity [10,11]:

$$\mathscr{R}^{\rm ECO} = \exp\left[-i\frac{\omega}{\pi T_{\rm QH}}\ln(\gamma|\omega|)\right]\exp\left(-\frac{|\omega|}{2T_{\rm QH}}\right), \tag{30}$$

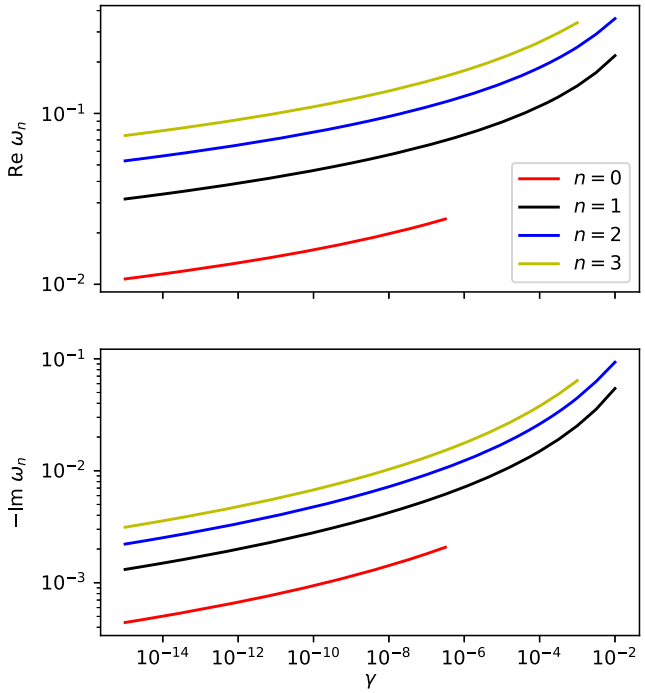


FIG. 9. Real and imaginary parts of QNMs for an irrotational ECO as functions of $\gamma$. They are the solutions to Eq. (31). The Boltzmann reflectivity is used, assuming $T_{\mathrm{QH}} = T_H$. Each mode is labeled with the overtone index $n$. The imaginary part of the QNMs is negative, meaning that the mode is stable.

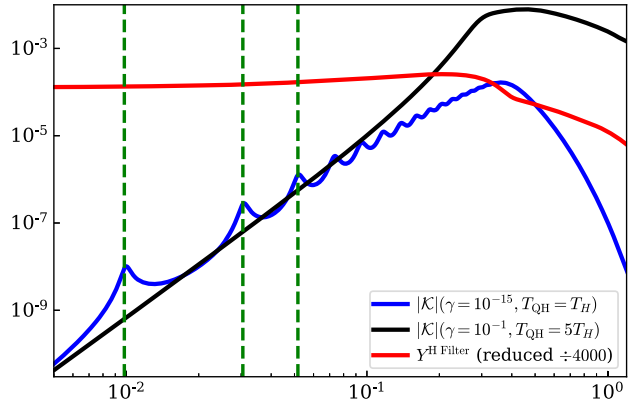


FIG. 10. Transfer function $\mathcal{K}$ of the ECO using $(\gamma = 10^{-15}, T_{\mathrm{QH}} = T_H)$ (blue curve) and $(\gamma = 10^{-1}, T_{\mathrm{QH}} = 5T_H)$ (black curve). The QNM resonances are visible in the former case, where the locations of the first three resonances are labeled with the dashed vertical lines, based on the estimation in Eq. (33). By comparison, the red curve corresponds to the absolute value of the filtered horizon wave $Y^{\mathrm{H\,Filter}}$ for SXS:BBH:0207 assuming that $v_\Sigma^{\mathrm{H}} = -13$ and $\Delta v = 2/\kappa$ [see Eq. (36)]. Its value is decreased by a factor of 4000 for simplicity.

where the quantity $T_{\mathrm{QH}}$ is the effective horizon temperature. The first term on the right-hand side of Eq. (30) implies that, as $\gamma \ll 1$, the region between $r_* \sim \frac{\ln\gamma}{2\pi T_{\mathrm{QH}}}$ and the peak of the BH potential forms a cavity. In this way, the ECO's QNM frequencies $\omega_n$ are determined as poles of the transfer function $\mathcal{K}(\omega)$ [see Eq. (27)],

$$\mathscr{R}^{\mathrm{ECO}}(\omega_n)\mathcal{R}^{\mathrm{BHT}}(\omega_n) = 1. \tag{31}$$

We solve Eq. (31) numerically and plot the value of $\omega_n$ as a function of $\gamma$ in Fig. 9, where the quantum horizon temperature $T_{\mathrm{QH}}$ is set as the Hawking temperature $T_H$:

$$T_H := \frac{\kappa}{2\pi} = \frac{1}{8\pi}, \tag{32}$$

with $\kappa = 1/4$ the surface gravity. We can see that the absolute value of the real and imaginary parts of $\omega_n$ increases with $\gamma$ and $n$. In particular, the negative sign of $\mathrm{Im}\omega_n$ ensures the stability of the QNMs. For the fundamental mode $n = 0$, the decay rate is less than $10^{-3}$; hence, it is long-lived.

This feature of the ECO QNMs is also visible in the transfer function $\mathcal{K}$, as shown in Fig. 10. The blue curve corresponds to the case with $\gamma = 10^{-15}$ and $T_{\mathrm{QH}} = T_H$. There are a number of local maxima (resonances) whose locations are close to the real part of the corresponding QNMs. In the limit of $\gamma \ll 1$, the peak frequency $\omega_{\mathrm{peak}}^{(n)}$ is given by

$$\omega_{\mathrm{peak}}^{(n)} = \omega_{\mathrm{FSR}}^{(n)} - \frac{\omega_{\mathrm{FSR}}^{(n)}}{(2n+1)\pi}\mathrm{Im}\ln[\mathcal{R}^{\mathrm{BHT}}(\omega_{\mathrm{FSR}}^{(n)})], \tag{33}$$

where the free spectral range (FSR) of the cavity is written as

$$\omega_{\mathrm{FSR}}^{(n)} = (2n+1)\frac{T_{\mathrm{QH}}\pi^2}{|\ln\gamma|}\left\{1 - \frac{1}{\ln\gamma}\ln\left[(2n+1)\frac{T_{\mathrm{QH}}\pi^2}{|\ln\gamma|}\right]\right\} + \mathcal{O}[(\ln\gamma)^{-2}], \quad n = 0, 1\ldots. \tag{34}$$

In Fig. 10 we label the location of $\omega_{\mathrm{peak}}^{(n)}$ for $n = 0, 1, 2$ using dashed vertical lines. Additionally, $\mathcal{K}$ has a global maximum at the fundamental QNM of a Schwarzschild BH $(0.374 - 0.0890i)$ that is contributed by the factor $1/D_{22}^{\mathrm{out}}$ (see the blue curve in Fig. 2). Within the frequency band $\omega < 0.374$, $\mathcal{K}$ is dominated by $1/D_{22}^{\mathrm{out}}$; hence, its asymptotic behavior is $\sim\omega^4$ as $\omega \to 0$. Conversely, for the band $\omega > 0.374$, $\mathcal{K}$ decays exponentially due to the second term on the right-hand side of Eq. (30).

On the other hand, when $\gamma$ is comparable to 1, GWs cannot be effectively trapped near the ECO surface, and the ECO QNMs do not exist. This fact is clearly manifested in the transfer function of the case with $\gamma = 10^{-1}$ and $T_{\mathrm{QH}} = 5T_H$, which is shown as a black curve in Fig. 10. Moreover, since the value of $T_{\mathrm{QH}}$ is greater than the previous one, more high-frequency contents can be reflected by the ECO surface, and hence emerge at infinity.

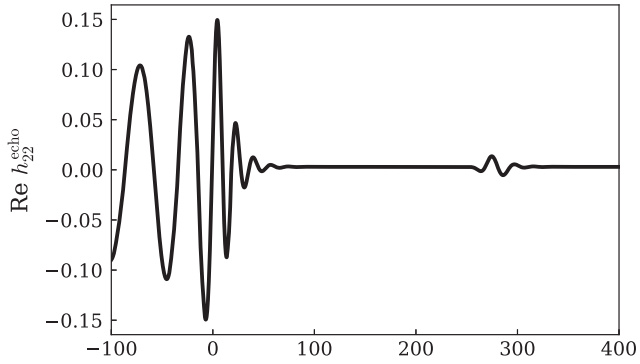


FIG. 11. Echo emitted by SXS:BBH:0207 following the main GW. Here we set $v_\Sigma^{(\mathrm{H})} = -13, \Delta v = 2/\kappa = 8, \gamma = 10^{-15}$, and $T_{\rm QH} = T_H$.

### C. Numerical computation of echo waveforms

In order to use Eq. (26) to compute echo waveforms, we first need to estimate the actual wave $Y_{lm\omega}^{\mathrm{H\,in\,ECO}}$ [see Eq. (23)], which falls down along the future horizon. In the context of the hybrid method, the future horizon exists partially in region I + II, except that the late-time portion of $Y_{lm}^{\mathrm{H\,in}}$ [see Eq. (14)] can represent $Y_{lm}^{\mathrm{H\,in\,ECO}}$; namely,

$$Y_{lm}^{\mathrm{H\,in\,ECO}}(v) = Y_{lm}^{\mathrm{H\,in}}(v), \quad \text{when } v > v_\Sigma^{(\mathrm{H})}. \tag{35}$$

Note again that the condition is in the time domain. The value of $v_\Sigma^{(\mathrm{H})}$ was determined by searching for the starting time after which $Y_{lm}^{\mathrm{H\,in}}(v)$ can be decomposed as a sum of the QNM overtones, as discussed in Sec. IV B. In practice, we impose the condition in Eq. (35) via a filter as follows:

$$\begin{aligned} Y_{lm}^{\mathrm{H\,in\,ECO}}(v) &\to Y_{lm}^{\mathrm{H\,Filter}}(v), \\ &= Y_{lm}^{\mathrm{H\,in}}(v)\mathcal{F}(v) + \mathrm{const} \times [1 - \mathcal{F}(v)], \end{aligned} \tag{36}$$

where the Planck-taper filter $\mathcal{F}(v)$ is given by [119]

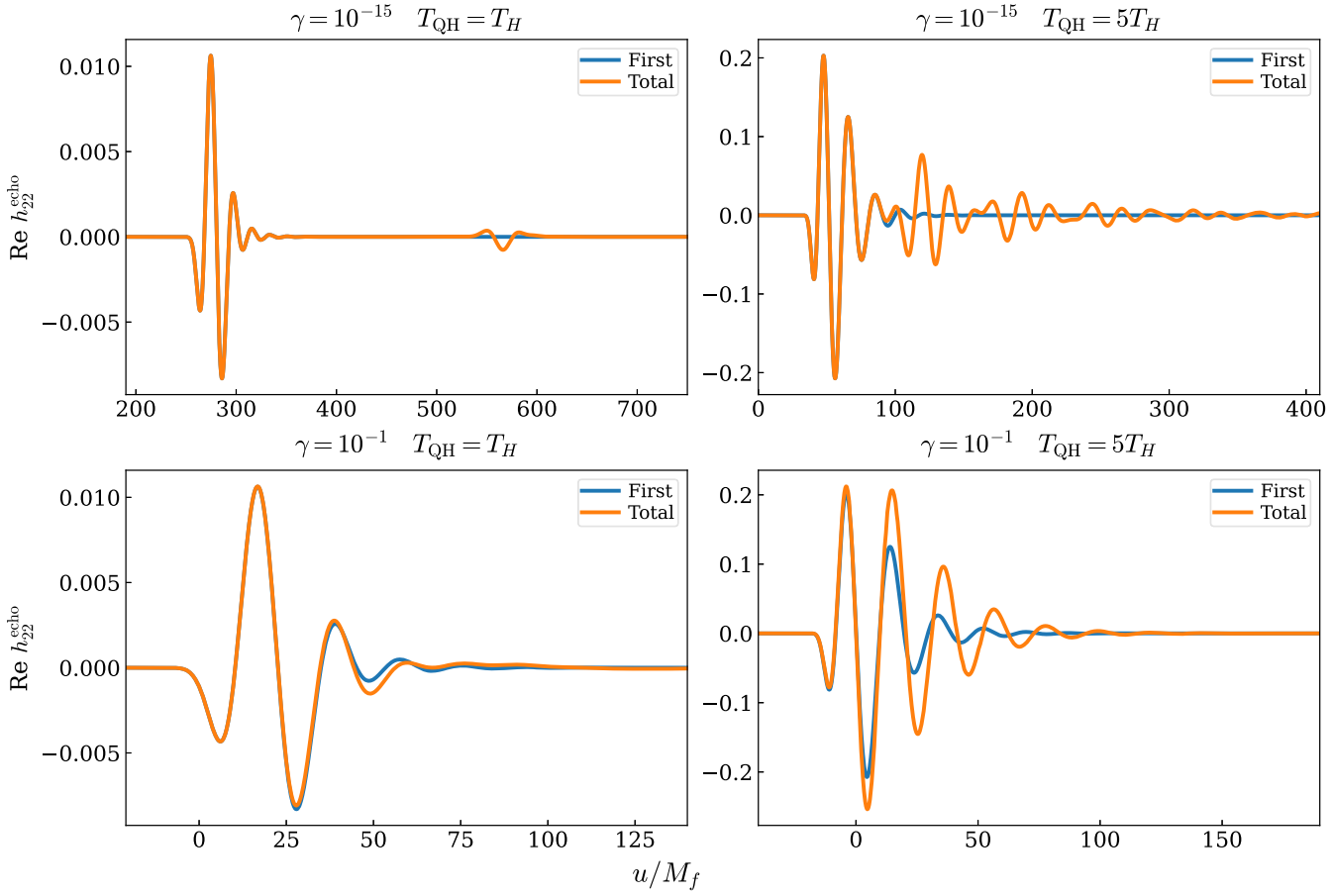


FIG. 12. The echoes emitted by SXS:BBH:0207, with a variety of $T_{\rm QH}$ and $\gamma$. The width of filter $\Delta v$ is equal to $2/\kappa$. The total echoes (orange curves) are compared to the first echoes (blue curves). In the upper-left panel, the values of $T_{\rm QH}$ and $\gamma$ are small enough that the spacing between echoes is greater than the echo duration; hence, the individual pulses are well separated, whereas in the other three panels different pulses overlap and interfere with each other.

$$\mathcal{F}(v; v_\Sigma^{(\mathrm{H})}, \Delta v) = \begin{cases} 0, & v < v_\Sigma^{(\mathrm{H})} - \Delta v, \\ \frac{1}{\exp z + 1}, & v_\Sigma^{(\mathrm{H})} - \Delta v < v < v_\Sigma^{(\mathrm{H})}, \\ 1, & v > v_\Sigma^{(\mathrm{H})}, \end{cases} \quad (37)$$

and $z = \frac{\Delta v}{v - v_\Sigma^{(\mathrm{H})}} + \frac{\Delta v}{v - v_\Sigma^{(\mathrm{H})} + \Delta v}$. The Planck-taper filter $\mathcal{F}(v)$ is a function that gradually ramps up from 0 to 1 within the time interval $[v_\Sigma^{(\mathrm{H})} - \Delta v, v_\Sigma^{(\mathrm{H})}]$. Therefore, $Y_{lm}^{\mathrm{H\,Filter}}(v)$ in Eq. (36) represents a quantity that switches from a constant value to $Y_{lm}^{\mathrm{H\,in}}(v)$ that is predicted by the hybrid method. The value of the constant does not affect the echo waveform, since this zero-frequency content cannot penetrate the BH potential (see the value of $D_{22}^{\mathrm{out}}$ in Fig. 2). In our case, we set the constant to 0.

With the transfer function at hand, we are able to compute echo waveforms. Figure 11 shows an echo signal following the main GW, emitted by the system SXS:BBH:0207, assuming that $v_\Sigma^{(H)} = -13$ (as summarized in Table II), $\Delta v = 2/\kappa = 8$, $\gamma = 10^{-15}$, and $T_{\mathrm{QH}} = T_H$. To further investigate how the echo signal is impacted by the parameters $(\gamma, T_{\mathrm{QH}})$, we vary their values and exhibit the results in Fig. 12. The echo waveform of SXS:BBH:1936 looks similar to that of SXS:BBH:0207, and it can be found in Appendix C. The total echo waveform is compared to the first echo. In the case of $\gamma = 10^{-15}$ and $T_{\mathrm{QH}} = T_H$ (shown in the upper-left panel), distinct echo pulses are separated by an equal time interval of

$$\Delta u^{\mathrm{echo}} \sim |\ln \gamma|/(\pi T_{\mathrm{QH}}), \quad (38)$$

which is long compared to the duration of the BBH ringdown. These well-separated echoes result mathematically from a collective excitation of the ECO's multiple QNMs displayed in Fig. 10—even though each individual QNM bears little resemblance to the echo pulse. On the other hand, for greater values of $T_{\mathrm{QH}}$ and $\gamma$ ($\gamma = 10^{-1}$ and $T_{\mathrm{QH}} = 5T_H$; shown in the lower-right panel), the spacing between nearby pulses becomes comparable to the pulse duration, distinct echo pulses interfere with each other, and we cannot resolve any single pulse. In addition, since the ECO with greater $T_{\mathrm{QH}}$ reflects a broader frequency band, the final echo is stronger.

We then investigate the impact of the filter parameter $\Delta v$ in Eq. (37). As shown in Fig. 13, we compute the first echo emitted by SXS:BBH:0207, using $(\gamma = 10^{-15}, T_{\mathrm{QH}} = T_H)$ and $v_\Sigma^{(\mathrm{H})} = -13$, for a variety of $\Delta v$. We can see that the waveforms have different amplitude evolutions within the first two cycles, but the distinction is suppressed shortly afterward.

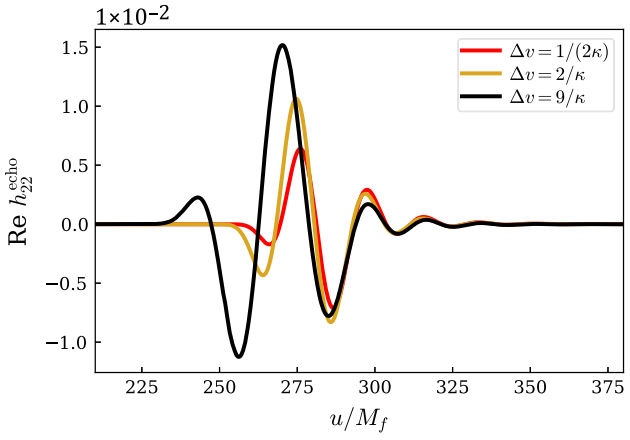


FIG. 13. The influence of the filter parameter $\Delta v$ on echo waveforms. Each curve corresponds to the real part of the first echo (with different $\Delta v$), using SXS:BBH:0207 and the Boltzmann reflectivity ($\gamma = 10^{-15}$ and $T_{\mathrm{QH}} = T_H$). The filter is applied at the future horizon with $v_\Sigma^{(\mathrm{H})} = -13$.

### D. Comparison with the inside prescription

The horizon filter is absent in the framework of the inside prescription [10,64]. Taking $v_\Sigma^{(\mathrm{H})} \to -\infty$, Eq. (35) reduces to

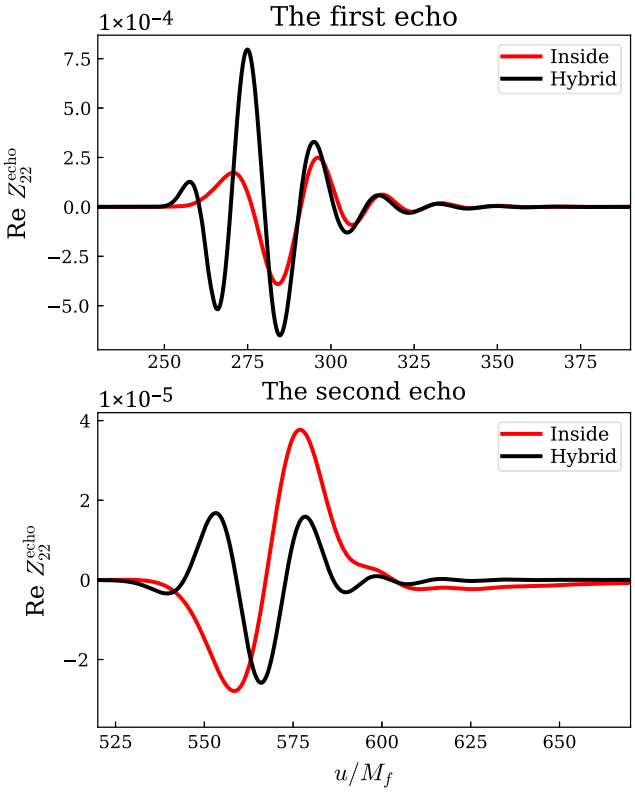


FIG. 14. Comparison between the hybrid approach and the inside prescription using SXS:BBH:0207. We choose a Boltzmann reflectivity with $\gamma = 10^{-15}$ and $T_{\mathrm{QH}} = T_H$. The upper panel shows the first echo, whereas the bottom panel displays the second echo. The filter is applied at null infinity (red curve labeled "Inside") and at the future horizon (black curve labeled "Hybrid"). The width of both filters $\Delta v$ is $2/\kappa$.

$$Y^{\mathrm{H\,in\,ECO}}_{lm\omega} = C^{\mathrm{in}}_{lm}(\omega) Y^{\infty}_{lm\omega} \tag{39}$$

and Eq. (26) becomes

$$Z^{\infty\,\mathrm{echo}}_{lm\omega} = \sum_{n=1}^{\infty} (\mathscr{R}^{\mathrm{ECO}} \mathcal{R}^{\mathrm{BH\,T}})^n Z^{\infty}_{lm\omega}, \tag{40}$$

where we have used the TS identities in Eqs. (9). A direct usage of Eq. (40) will lead to undesired low-frequency contents contributed by the inspiral stage. A work-around would be taking only the ringdown portion of $Z^{\infty}_{lm}(u)$, following Ref. [64]. We compare the hybrid method [Eq. (26)] to the inside formula [Eq. (40)] in Fig. 14, assuming SXS:BBH:0207. Here we choose $\Delta v = 2/\kappa$, $\gamma = 10^{-15}$, and $T_{\mathrm{QH}} = T_H$. We see that for the first echo the hybrid method leads to a stronger signal, but the inside prescription has a stronger second echo. Meanwhile, for the initial part of the first echo, the hybrid method gives rise to one more cycle, but the evolution is almost identical afterward.

## VI. DETECTABILITY AND PARAMETER ESTIMATION

In this section, we focus on the detectability of the echoes computed in this paper by current and future detectors. We first give a brief summary of the detector response, signal-to-noise ratio (SNR), and Fisher-matrix calculations in Sec. VI A. Then we study the detectability of echoes by calculating the SNR in Sec. VI B and discuss the parameter estimation by adopting the Fisher matrix in Sec. VI C.

### A. The signal-to-noise ratio and Fisher-matrix formalism

We first construct two polarizations of an echo $h^{\mathrm{echo}}_{+,\times}$ by assembling $h^{\mathrm{echo}}_{lm}$:

$$h^{\mathrm{echo}}_{+} - i h^{\mathrm{echo}}_{\times} = \sum_{m=\pm 2} {}_{-2}Y_{l=2,m}(\theta,\phi) h^{\mathrm{echo}}_{l=2,m}, \tag{41}$$

where we use the leading contributions $h^{\mathrm{echo}}_{2,\pm 2}$, which satisfy the condition $h^{\mathrm{echo}}_{2,-2} = (h^{\mathrm{echo}}_{2,2})^*$. The echo strain $h^{\mathrm{echo}}$ detected by a detector is given by

$$h^{\mathrm{echo}} = F_+(\theta_S,\phi_L,\psi_L) h^{\mathrm{echo}}_{+} + F_\times(\theta_S,\phi_L,\psi_L) h^{\mathrm{echo}}_{\times}, \tag{42}$$

with $(\theta_S,\phi_L)$ the sky location of a source with respect to the detector and $\psi_L$ the polarization angle. The SNR of a given GW signal $h$ is written as $\sqrt{(h|h)}$, where the inner product between the two waveforms $(h|g)$ reads

$$(h|g) = 4\mathrm{Re}\int \frac{h^*(f) g(f)}{S_n(f)} df. \tag{43}$$

Here $S_n(f)$ is the spectral density of the noise when it detects GWs. The averaged SNR over angular parameters $(\theta_S,\phi_L,\psi_L,\theta,\phi)$ is given by [120]

$$\langle \rho^2 \rangle = \frac{16}{25}\int \frac{|h_+|^2(\theta=0)}{S_n(f)} df. \tag{44}$$

We shall adopt the sky-averaged SNR throughout this paper.

On the other hand, the Fisher matrix for a given gravitational waveform $h(\lambda^i)$ can be written as

$$\Gamma_{ij} = \left(\frac{\partial h}{\partial \lambda^i}\middle|\frac{\partial h}{\partial \lambda^j}\right), \tag{45}$$

where $\lambda^i$ are parameters to be estimated. In this paper, we restrict ourselves to $\gamma$ and $T_{\mathrm{QH}}$ values that determine the Boltzmann reflectivity [Eq. (30)]. By inverting $\Gamma_{ij}$, we obtain the parameter estimation accuracies for $\lambda^i$,

$$\Delta\lambda^i = \sqrt{(\Gamma^{-1})_{ii}}. \tag{46}$$

### B. Detectability of echoes

To study how the SNR is impacted by the reflectivity parameters ($\gamma$ and $T_{\mathrm{QH}}$), we adopt an aLIGO-like detector [121] and a Cosmic Explorer (CE)-like detector [122] for both SXS:BBH:0207 and SXS:BBH:1936. We assume the binaries to have a total mass of 60 $M_\odot$ and to be located 100 Mpc from the detector.

In the baseline case with $T_{\mathrm{QH}} = T_H$, $\gamma = 10^{-1}$, and $\Delta v = 2/\kappa$ and using the values of $v^{(\mathrm{H})}_{\Sigma}$ given in Table II, we obtain (sky-averaged) echo SNRs of ∼0.45 for aLIGO and ∼15 for CE. The echo SNRs of SXS:BBH:1936 are greater than those of SXS:BBH:0207 by a factor of ∼1.5 in both detectors. In order to make a comparison with Ref. [58], we also estimate the ratios between the echo SNR and the ringdown SNR. To first obtain the ringdown SNR, we choose the lower limit of integration in Eq. (44) to be the frequency of $h^{\infty}_{22}$ evaluated at $u^{(h)}$ [see Eq. (17a) and Table II]. For aLIGO, the ringdown SNR for SXS:BBH:0207 is around 7.0 and the ratio $\mathrm{SNR}_{\mathrm{echo}}/\mathrm{SNR}_{\mathrm{ringdown}} = 6.5\%$, which is close to the blue curve in the bottom-left panel of Fig. 9 in Ref. [58].

In Fig. 15, we explore how the echo SNR depends on values of $\gamma$ and $T_{\mathrm{QH}}$, for both detectors and both binaries, respectively, assuming that $\Delta v = 2/\kappa$ and using values of $v^{(\mathrm{H})}_{\Sigma}$ listed in Table II. The SNR increases with $T_{\mathrm{QH}}$ since a larger $T_{\mathrm{QH}}$ corresponds to a broader reflection frequency band, and more incident waves are reflected. The $\gamma$ dependence of SNR is more complex. For small values of $T_{\mathrm{QH}}$ (i.e., those around unity, as originally proposed by Wang *et al.* [10]), the SNR barely depends on $\gamma$ because in this case the echoes are weak and dominated mainly by the

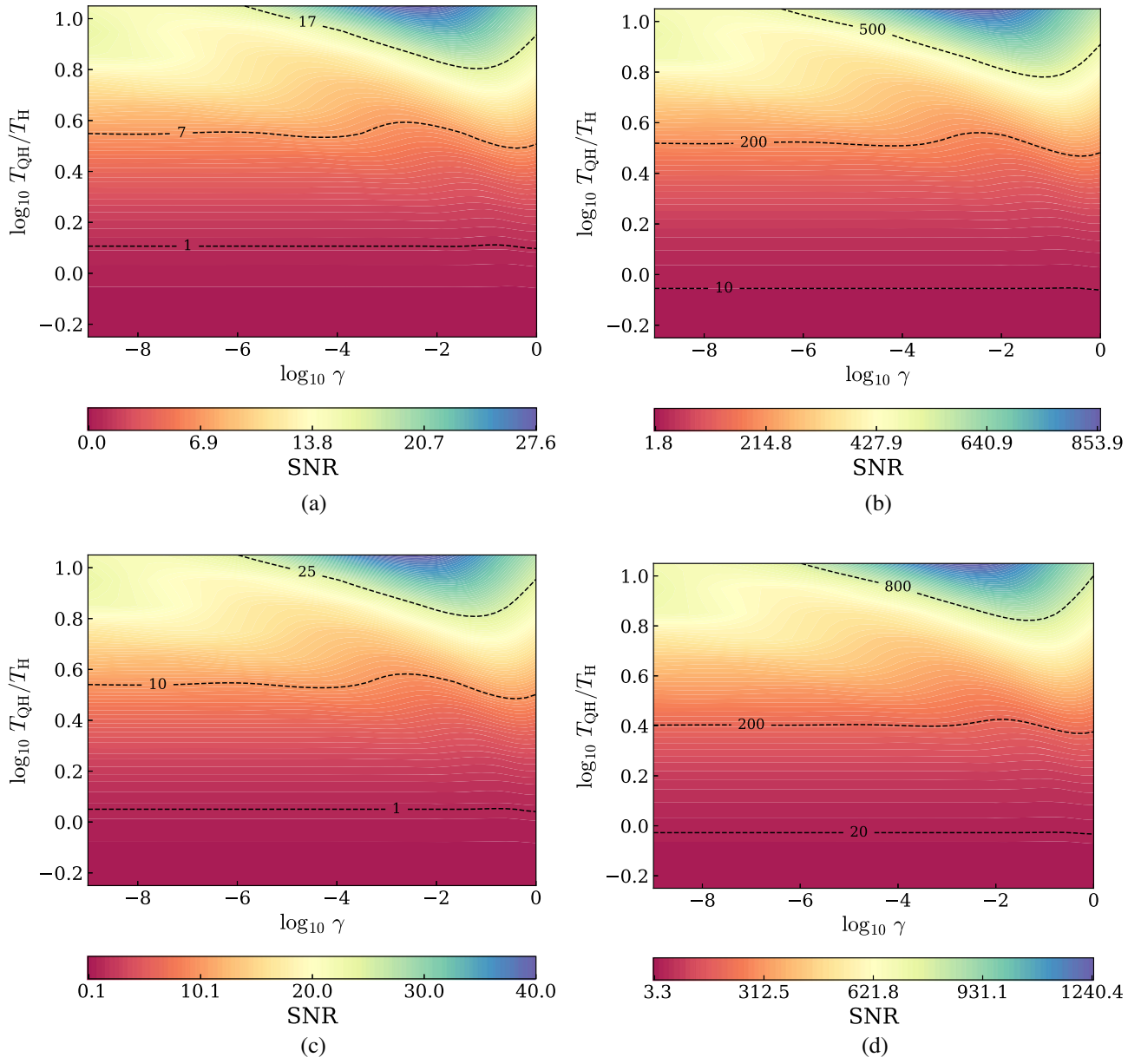


FIG. 15. Sky-averaged echo SNR across the $T_{\rm QH} - \gamma$ space using SXS:BBH:0207 (upper panels) and SXS:BBH:1936 (lower panels), as well as aLIGO (left column) and CE (right column). The binary system is 100 Mpc from the detector, with a total mass of 60 $M_\odot$. We set $\Delta v$ to $2/\kappa$, and the values of $v_\Sigma^{(\rm H)}$ are listed in Table II.

first pulse, where $\gamma$ controls only the separation between the echoes in time, meaning that it does not affect the SNR. By contrast, for $T_{\rm QH} \gtrsim 5T_H$, the echoes may overlap with each other and (constructively) interfere, thereby elevating the SNR.

Next we investigate the impact of filters on the horizon—namely, the advanced time $v_\Sigma^{(\rm H)}$ at which the shell $\Sigma$ crosses the horizon—and the thickness $\Delta v$ of the transition region in which we cut off reflection. Taking SXS:BBH:0207 and CE, for example, we plot in Fig. 16 the sky-averaged echo SNR as a function of two filter parameters $v_\Sigma^{(\rm H)}$ and $\Delta v$ [see Eq. (37)], where we choose $\gamma = 10^{-15}$ and $T_{\rm QH} = T_H$. As expected, the SNR decreases as either $v_\Sigma^{(\rm H)}$ increases or $\Delta v$ decreases. The global pattern suggests that the dependence on $v_\Sigma^{(\rm H)}$ and $\Delta v$ is linearly correlated.

### C. Parameter estimation

We now use the Fisher-matrix formalism to study the parameter estimation. Here we restrict ourselves to the reflectivity parameters ($\gamma$ and $T_{\rm QH}$) resulting in 2D Fisher matrices. This will result in an underestimate of the measurement errors. As shown in Fig. 17, we compute the fractional errors of $T_{\rm QH}$ and $\gamma$ using SXS:BBH:0207.

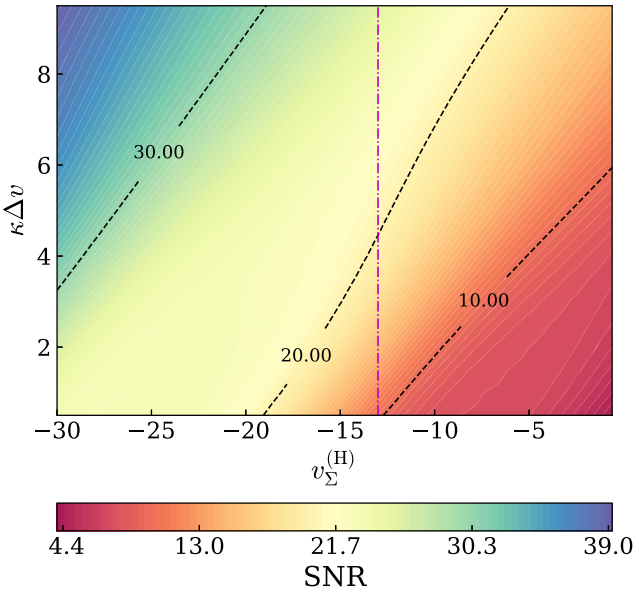


FIG. 16. Sky-averaged echo SNR as a function of filter parameters $v_\Sigma^{(H)}$ and $\Delta v$ [see Eq. (37)] using CE. The binary system is SXS:BBH:0207 and has the same total mass and distance as Fig. 15. We use the Boltzmann reflectivity with $\gamma = 10^{-15}$ and $T_{QH} = T_H$. The vertical dash-dotted line represents the value of $v_\Sigma^{(H)}$ given in Table II.

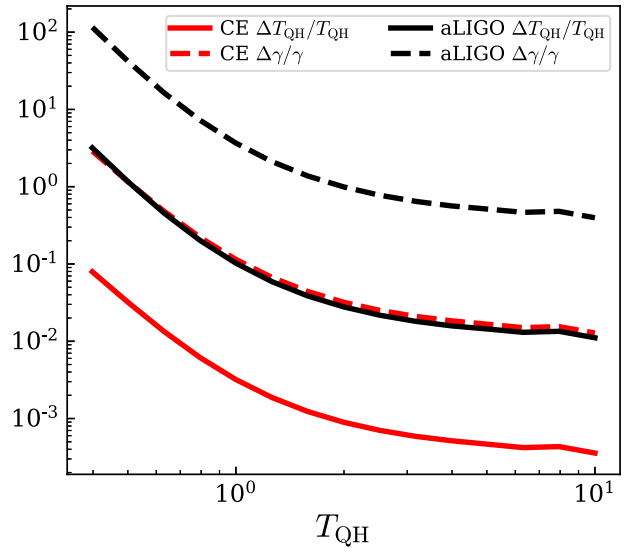


FIG. 17. Fractional error of $T_{QH}$ (solid curves) and $\gamma$ (dashed curves) as functions of $T_{QH}$ using aLIGO (black curves) and CE (red curves). The binary system is SXS:BBH:0207, which has a total mass of 60 $M_\odot$ and is located 100 Mpc from the detector. The two filter parameters $v_\Sigma^{(H)}$ and $\Delta v$ are still set to $-13$ and $2/\kappa$, respectively. We vary the value of $T_{QH}$ from 0.4 to 10 while fixing the value of $\gamma$ at $10^{-15}$.

We still assume that the system has a total mass of 60 $M_\odot$ and a location 100 Mpc from the detector. The two filter parameters $v_\Sigma^{(H)}$ and $\Delta v$ are still set at $-13$ and $2/\kappa$, respectively. We vary the value of $T_{QH}$ from 0.4 to 10 while fixing the value of $\gamma$ at $10^{-15}$. We see that the fractional error decreases as $T_{QH}$ increases since the echo signal is stronger. The constraint on $T_{QH}$ is greater than $\gamma$ since it has a greater impact on the echo's profile and SNR. When we choose $T_{QH} = T_H$, aLIGO can constrain $\gamma$ and $T_{QH}$ to the level of 366.7% and 10.2%, respectively. These two constraints lead to 20.9% measurement uncertainty in the time interval $\Delta u^{echo}$ between individual echoes based on Eq. (38). For CE, the fractional errors of $\gamma$, $T_{QH}$, and $\Delta u^{echo}$ are 11.4%, 0.3%, and 0.65%, respectively.

## VII. CONCLUSION

In this paper, we made use of the hybrid method [77,78] to establish an echo waveform model for comparable-mass merging binaries whose remnants do not rotate. The hybrid method was originally proposed to predict GWs emitted by BBH coalescences—it separates the spacetime of a BBH event into an inner PN region and an outer BHP region (see Fig. 1). The two regions communicate via boundary conditions on a world tube $\Sigma$. To build the echo model, we first took the Weyl scalars of the BBH systems from CCE [83] at future null infinity. Then we *reversed* the process of the hybrid method by evolving Weyl scalars back into the bulk, and the solution in the BHP region was proportional to the up-mode solution to the homogeneous Teukolsky equation, as required by the uniqueness of the solutions. With the solution at hand, we were able to compute the GW that falls down along the future horizon.

Since the BHP theory is not valid inside the matching shell $\Sigma$, only the portion of GW that lies outside the world tube $\Sigma_{Shell}$ is physical. Consequently, the usefulness of our method is limited to the ringdown phase. We determined the location of $\Sigma$ (namely, the advanced time $v_\Sigma^{(H)}$ at which it crosses the future horizon) by looking for the quasinormal ringing regime of the horizon—$\psi_0$; we fitted $Y_{lm}^{H\,in}$ to a superposition of five overtones [Eq. (17)]. We then removed the earlier piece of $\psi_0$ (with $v < v_\Sigma^{(H)}$) by applying a Planck-taper filter whose width $\Delta v$ (a free parameter in our model) can be viewed as the effective thickness of the matching shell.

Next, by utilizing the physical boundary condition near the ECO surfaces [61] and the Boltzmann reflectivity [10], we computed the QNMs of irrotational ECOs, as well as echo signals of two systems, SXS:BBH:0207 and SXS:BBH:1936. We picked these two runs because their remnant spins vanish. The prediction made using the hybrid method for ringdown signals proved to be accurate in this

case [77]. Finally, we studied the detectability and parameter estimation of the echoes.

We summarize our main conclusions as follows:

(i) The hybrid method is similar to the inside prescription of Refs. [10,64] in the sense that both of them treat the main GW as a transmitted wave of an initial pulse emerging from the past horizon (see Fig. 4). Furthermore, filters are involved in both treatments, which, however, have different physical interpretations. The inside prescription (also the CLA) handles the system as an initial value problem (the Cauchy problem), where the entire process is split into two stages. Only the late-time portion lies in the BHP region. Therefore, the filter needs to be applied at future null infinity. Conversely, in our case, the exterior system is described by a boundary value problem—a spatial volume is separated at every moment. Accordingly, the filter is imposed at the future horizon to remove the unrealistic portion of the incoming GW. We took SXS:BBH:0207 as an example and compared the hybrid method with the inside prescription. We found that the inside prescription leads to fewer cycles than the hybrid method for the initial part of the echo. Meanwhile, the first echo predicted using the inside prescription is weaker than the result using the hybrid method.

(ii) The Weyl scalars $\psi_{0,4}$ from CCE are consistent with the TS identities throughout the entire frequency band in question. This supports the treatment of the hybrid method that uses BHP theory to describe the exterior region, at least when the remnant object does not rotate.

(iii) As in the studies of Refs. [110,115], using six overtones, the ringdown of the strain for SXS:BBH:1936 starts $2M_f$ after the peak. However, the time for SXS:BBH:0207 can be extended to $\sim 11M_f$ before the peak. For the horizon and infinity $\psi_0$: $Y_{22}^{\mathrm{H}/\infty}$, the prediction made using CCE is less accurate, and we were only able to resolve five overtones. The linearly quasinormal ringing regimes of $Y_{22}^{\mathrm{H\,in}}$ for SXS:BBH:0207 and SXS:BBH:1936 are similar, and they start at $\sim 13M_f$–$15M_f$ before the peak.

We restricted ourselves to inspiraling compact binaries whose remnants are Schwarzschild-like ECOs. Future work could extend the hybrid method to Kerr-like ECOs and utilize it to compute echoes emitted by more general comparable-mass coalescence systems. It is worth pointing out that, throughout the process, the Kerr-like background should have an adiabatically evolving mass and angular momentum due to GW emission. It will be a limitation for the hybrid method if one fails to capture this feature. Another possible avenue for future work is to apply our calculations to head-on collisions and compare the echo waveform with the results in Ref. [75].

## ACKNOWLEDGMENTS

We thank Manu Srivastava, Shuo Xin, Rico K. L. Lo, and Ling Sun for the discussions. This work makes use of the Black Hole Perturbation Toolkit. The computations presented here were conducted on the Caltech High Performance Cluster, partially supported by a grant from the Gordon and Betty Moore Foundation. This work was supported by the Simons Foundation (Grant No. 568762), the Brinson Foundation, and the Sherman Fairchild Foundation, and by NSF Grants No. PHY-2011961, No. PHY-2011968, No. PHY-1836809, and No. OAC-1931266 at Caltech, and NSF Grants No. PHY-1912081 and No. OAC-1931280 at Cornell.

## APPENDIX A: THE QNM AMPLITUDES OF SXS:BBH:0207 AND SXS:BBH:1936

Figure 18 shows the absolute value and phase of $\mathcal{A}_n^{(\mathrm{h}/\infty/\mathrm{H})}$ and $\mathcal{B}_n^{(\mathrm{h}/\infty/\mathrm{H})}$ [see Eq. (17)]. For SXS:BBH:1936, $\mathcal{A}_n^{(h)}$ peaks at $n = 5$, which is consistent with previous studies [110,115,116]. However, in this case the absolute value of the retrograde mode $\mathcal{B}_n^{(h)}$ is comparable to that of $\mathcal{A}_n^{(h)}$; thus, it is not negligible. For SXS:BBH:0207, the contribution of the retrograde mode $\mathcal{B}_n^{(h)}$ is considerable as well, while $\mathcal{A}_n^{(h)}$ peaks at $n = 2$ and $\mathcal{B}_n^{(h)}$ peaks at $n = 3$.

## APPENDIX B: THE CHARACTERISTIC APPROACH TO SOLVING THE RW EQUATION

Equation (1) can be solved numerically via a second-order-accurate, characteristic method proposed by Gundlach *et al.* [123]. As shown in Fig. 19, Gundlach *et al.* [123] picked four points on a discretized $(u, v)$ grid:

$$
\begin{aligned}
&{}_s\Psi_{lm}^{\mathrm{N}} = {}_s\Psi_{lm}^{\mathrm{SN}}(u+h, v+h), \qquad {}_s\Psi_{lm}^{\mathrm{E}} = {}_s\Psi_{lm}^{\mathrm{SN}}(u, v+h),\\
&{}_s\Psi_{lm}^{\mathrm{W}} = {}_s\Psi_{lm}^{\mathrm{SN}}(u+h, v), \qquad {}_s\Psi_{lm}^{\mathrm{S}} = {}_s\Psi_{lm}^{\mathrm{SN}}(u, v),
\end{aligned} \tag{B1}
$$

with $h$ the step size. The value in the lower-left corner, ${}_s\Psi_{lm}^{\mathrm{W}}$, can be obtained using

$$
\begin{aligned}
{}_s\Psi_{lm}^{\mathrm{W}} = {}&{}_s\Psi_{lm}^{\mathrm{N}} + {}_s\Psi_{lm}^{\mathrm{S}} - {}_s\Psi_{lm}^{\mathrm{E}}\\
&+ \frac{h^2}{8} V_{\mathrm{RW}}^{l}(r_c)({}_s\Psi_{lm}^{\mathrm{N}} + {}_s\Psi_{lm}^{\mathrm{S}}) + \mathcal{O}(h^3),
\end{aligned} \tag{B2}
$$

where $V_{\mathrm{RW}}^{l}(r_c)$ is the value of the RW potential at the center, $r_c = (u + h/2, v + h/2)$. We note that Eq. (B2) is different from the one used in Refs. [77,78], where ${}_s\Psi_{lm}^{\mathrm{N}}$ was calculated based on the other three. This is because we evolve the system backward into the bulk (from $\mathcal{I}^+$ to the past horizon).

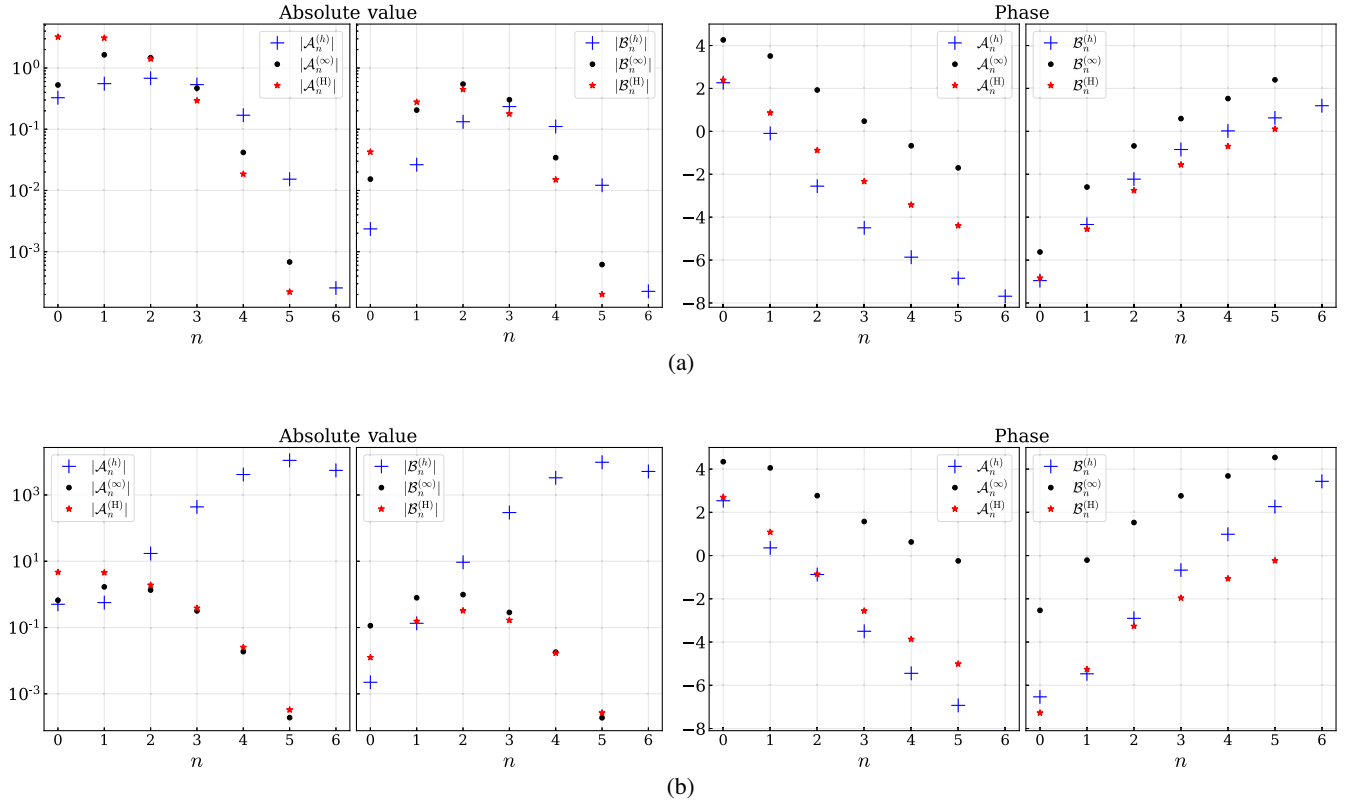


FIG. 18. Absolute value (left two panels) and phase (right two panels) of the prograde mode $\mathcal{A}_n$ and the retrograde mode $\mathcal{B}_n$ assuming that (a) SXS:BBH:0207 and (b) SXS:BBH:1936. We fit Eqs. (17) to the data of $h^{\infty}_{22}$ (blue), $Y^{\infty}_{22}$ (black), and $Y^{\mathrm{H\,in}}_{22}$ (red) obtained from CCE.

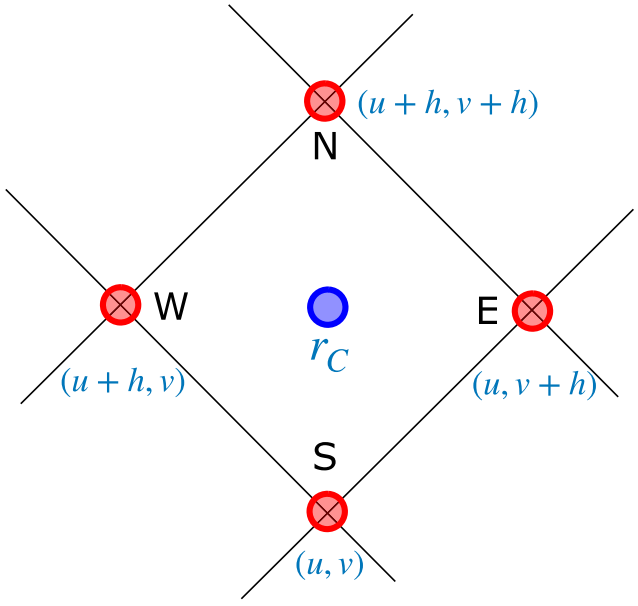


FIG. 19. The $(u, v)$ grid cell in a characteristic evolution scheme of the RW equation.

## APPENDIX C: SXS:BBH:1936

Using SXS:BBH:1936, we test the validity of the TS identity at the null infinity [see Eq. (9a)] in Fig. 20. Conventions are the same as in Fig. 6.

In Fig. 21, we present the total echo and the first echo with a variety of $\gamma$ and $T_{\mathrm{QH}}$ values. The location of the filter is listed in Table II, and the width of the filter is set at $2/\kappa$.

## APPENDIX D: CHANDRASEKHAR-SASAKI-NAKAMURA TRANSFORMATION

The generalized Chandrasekhar-Sasaki-Nakamura transformation reads [124]

$$ {}_s\Psi^{\mathrm{SN}}_{lm} = \begin{cases} r^{|s|+1} D_-^{|s|}\left(\frac{1}{r^{|s|}}\, {}_sR^{\mathrm{BH}}_{lm}\right) & s < 0, \\ r^{s+1} D_+^{s}\left[\left(\frac{\Delta}{r}\right)^{s} {}_sR^{\mathrm{BH}}_{lm}\right] & s \geq 0, \end{cases} \tag{D1a} $$

$$ {}_sR^{\mathrm{BH}}_{lm} = \begin{cases} \frac{1}{c_0}\left(\frac{\Delta}{r}\right)^{|s|} D_+^{|s|}\left(r^{|s|-1}\, {}_s\Psi^{\mathrm{SN}}_{lm}\right) & s \leq 0, \\ \frac{1}{c_0}\frac{1}{r^{s}} D_-^{s}\left(r^{s-1}\, {}_s\Psi^{\mathrm{SN}}_{lm}\right) & s > 0, \end{cases} \tag{D1b} $$

with $D_{\pm} = \frac{d}{dr} \pm \frac{i\omega r^2}{\Delta}$ and the constant $c_0$ given by

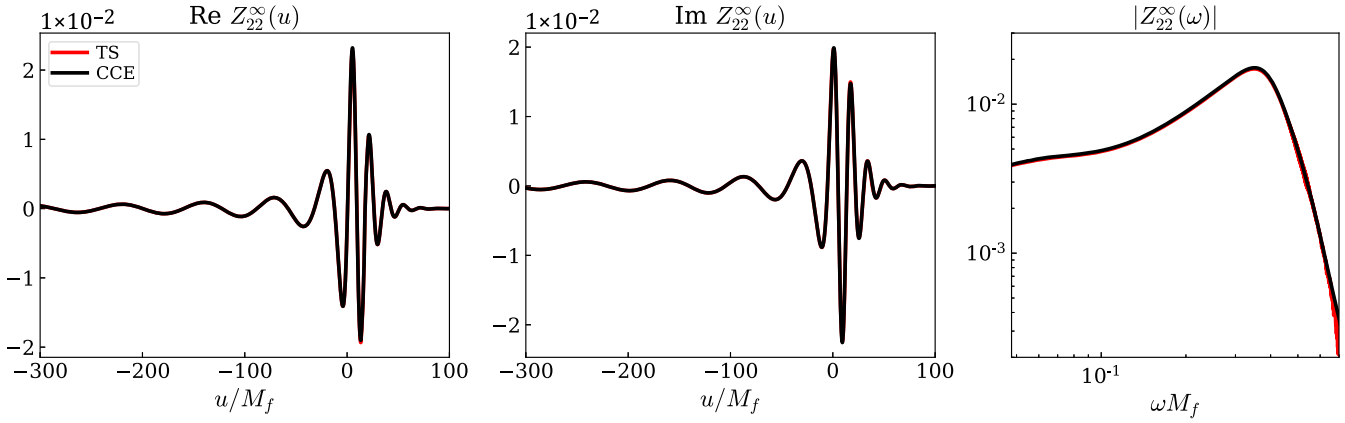


FIG. 20. Same as Fig. 6 using SXS:BBH:1936.

$$c_0 = \begin{cases} C^* & s = -2, \\ l(l+1) & s = \pm 1, \\ C & s = 2, \end{cases}$$

where $C$ is as defined in Eq. (10a).

The up-mode solution, ${}_s\Psi^{\rm up}_{lm\omega}$, to the RW equation [Eq. (1)] takes an asymptotic expansion

$${}_{-2}\Psi^{\rm up}_{lm\omega} \sim \begin{cases} B^{\infty}_{lm\omega} e^{i\omega r_*}, & r_* \to +\infty, \\ B^{\rm out}_{lm\omega} e^{i\omega r_*} + B^{\rm in}_{lm\omega} e^{-i\omega r_*}, & r_* \to -\infty, \end{cases} \tag{D2a}$$

$${}_{+2}\Psi^{\rm up}_{lm\omega} \sim \begin{cases} A^{\infty}_{lm\omega} e^{i\omega r_*}, & r_* \to +\infty, \\ A^{\rm out}_{lm\omega} e^{i\omega r_*} + A^{\rm in}_{lm\omega} e^{-i\omega r_*}, & r_* \to -\infty. \end{cases} \tag{D2b}$$

Plugging Eqs. (5) and (D2) into Eq. (D1), we obtain

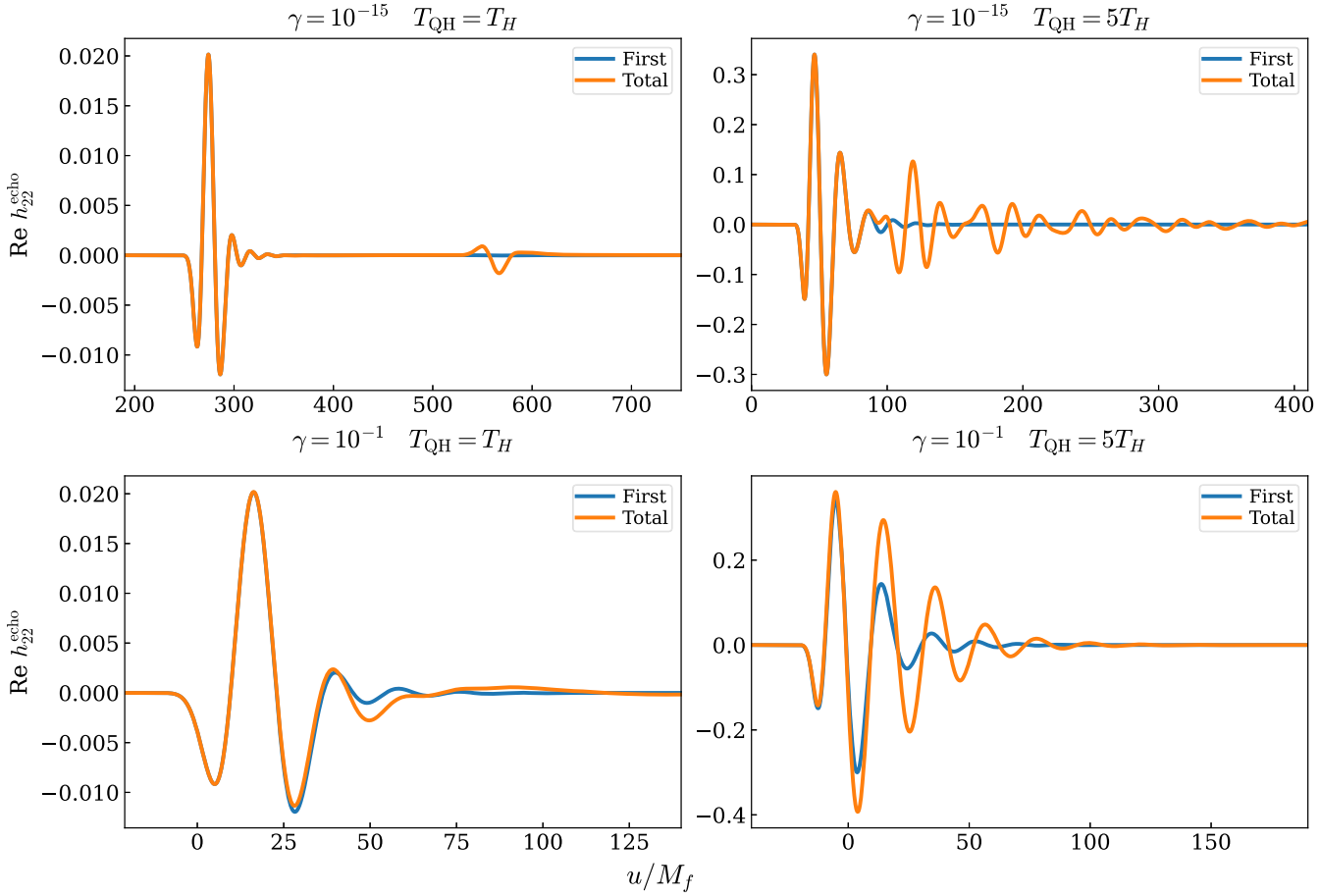


FIG. 21. Same as Fig. 12 using SXS:BBH:1936.

$$B^{\infty}_{lm\omega} = -\frac{C^*}{4\omega^2}, \qquad B^{\rm out}_{lm\omega} = -\frac{C^* D^{\rm out}_{lm}}{8\omega(i+4\omega)}, \qquad B^{\rm in}_{lm\omega} = 16(1-6i\omega-8\omega^2)D^{\rm in}_{lm},$$
$$A^{\infty}_{lm\omega} = -4\omega^2, \qquad A^{\rm in}_{lm\omega} = \frac{C}{8\omega(i-4\omega)} C^{\rm in}_{lm}, \qquad A^{\rm out}_{lm\omega} = 16(1+6i\omega-8\omega^2)C^{\rm out}_{lm}, \tag{D3a}$$

and the TS identity in Eq. (11) implies

$$\frac{B^{\rm in}_{lm\omega}}{B^{\infty}_{lm\omega}} = \frac{A^{\rm in}_{lm\omega}}{A^{\infty}_{lm\omega}}. \tag{D4}$$


[1] V. Cardoso, E. Franzin, and P. Pani, Phys. Rev. Lett. **116**, 171101 (2016); **117**, 089902(E) (2016).
[2] V. Cardoso, S. Hopper, C. F. B. Macedo, C. Palenzuela, and P. Pani, Phys. Rev. D **94**, 084031 (2016).
[3] V. Cardoso and P. Pani, Nat. Astron. **1**, 586 (2017).
[4] J. Zhang and S.-Y. Zhou, Phys. Rev. D **97**, 081501 (2018).
[5] R. Dong and D. Stojkovic, Phys. Rev. D **103**, 024058 (2021).
[6] A. Almheiri, D. Marolf, J. Polchinski, and J. Sully, J. High Energy Phys. 02 (2013) 062.
[7] S. B. Giddings, Classical Quantum Gravity **33**, 235010 (2016).
[8] N. Oshita and N. Afshordi, Phys. Rev. D **99**, 044002 (2019).
[9] V. Cardoso, V. F. Foit, and M. Kleban, J. Cosmol. Astropart. Phys. 08 (2019) 006.
[10] Q. Wang, N. Oshita, and N. Afshordi, Phys. Rev. D **101**, 024031 (2020).
[11] N. Oshita, Q. Wang, and N. Afshordi, J. Cosmol. Astropart. Phys. 04 (2020) 016.
[12] J. Abedi, L. F. L. Micchi, and N. Afshordi, arXiv:2201.00047.
[13] S. Chakraborty, E. Maggio, A. Mazumdar, and P. Pani, arXiv:2202.09111.
[14] K. Chakravarti, R. Ghosh, and S. Sarkar, Phys. Rev. D **104**, 084049 (2021).
[15] K. Chakravarti, R. Ghosh, and S. Sarkar, Phys. Rev. D **105**, 044046 (2022).
[16] P. O. Mazur and E. Mottola, Proc. Natl. Acad. Sci. U.S.A. **101**, 9545 (2004).
[17] M. Visser and D. L. Wiltshire, Classical Quantum Gravity **21**, 1135 (2004).
[18] T. Damour and S. N. Solodukhin, Phys. Rev. D **76**, 024016 (2007).
[19] B. Holdom and J. Ren, Phys. Rev. D **95**, 084034 (2017).
[20] S. D. Mathur, Fortschr. Phys. **53**, 793 (2005).
[21] V. Cardoso, P. Pani, M. Cadoni, and M. Cavaglia, Phys. Rev. D **77**, 124044 (2008).
[22] R. Vicente, V. Cardoso, and J. C. Lopes, Phys. Rev. D **97**, 084032 (2018).
[23] E. Maggio, P. Pani, and V. Ferrari, Phys. Rev. D **96**, 104047 (2017).
[24] E. Maggio, V. Cardoso, S. R. Dolan, and P. Pani, Phys. Rev. D **99**, 064007 (2019).
[25] P. V. P. Cunha, E. Berti, and C. A. R. Herdeiro, Phys. Rev. Lett. **119**, 251102 (2017).
[26] J. Keir, Classical Quantum Gravity **33**, 135009 (2016).
[27] V. Cardoso, L. C. B. Crispino, C. F. B. Macedo, H. Okawa, and P. Pani, Phys. Rev. D **90**, 044069 (2014).
[28] R. Ghosh and S. Sarkar, Phys. Rev. D **104**, 044019 (2021).
[29] B. Chen, Y. Chen, Y. Ma, K.-L. R. Lo, and L. Sun, arXiv:1902.08180.
[30] A. Addazi, A. Marcianò, and N. Yunes, Eur. Phys. J. C **80**, 36 (2020).
[31] V. Cardoso and P. Pani, Living Rev. Relativity **22**, 4 (2019).
[32] J. Abedi, N. Afshordi, N. Oshita, and Q. Wang, Universe **6**, 43 (2020).
[33] R. S. Conklin and N. Afshordi, arXiv:2201.00027.
[34] S. Mukherjee, S. Datta, S. Tiwari, K. S. Phukon, and S. Bose, arXiv:2202.08661.
[35] T. Regge and J. A. Wheeler, Phys. Rev. **108**, 1063 (1957).
[36] F. J. Zerilli, Ph.D. thesis, Princeton University, 1969.
[37] L. Hui, D. Kabat, and S. S. C. Wong, J. Cosmol. Astropart. Phys. 12 (2019) 020.
[38] M. H.-Y. Cheung, K. Destounis, R. P. Macedo, E. Berti, and V. Cardoso, Phys. Rev. Lett. **128**, 111103 (2022).
[39] Z. Mark, A. Zimmerman, S. M. Du, and Y. Chen, Phys. Rev. D **96**, 084002 (2017).
[40] A. Testa and P. Pani, Phys. Rev. D **98**, 044018 (2018).
[41] S. M. Du and Y. Chen, Phys. Rev. Lett. **121**, 051105 (2018).
[42] E. Maggio, L. Buoninfante, A. Mazumdar, and P. Pani, Phys. Rev. D **102**, 064053 (2020).
[43] V. Cardoso, A. del Rio, and M. Kimura, Phys. Rev. D **100**, 084046 (2019); **101**, 069902(E) (2020).
[44] M. Bianchi, D. Consoli, A. Grillo, J. F. Morales, P. Pani, and G. Raposo, Phys. Rev. Lett. **125**, 221601 (2020).
[45] I. Bena and D. R. Mayerson, Phys. Rev. Lett. **125**, 221602 (2020).
[46] T. Ikeda, M. Bianchi, D. Consoli, A. Grillo, J. F. Morales, P. Pani, and G. Raposo, Phys. Rev. D **104**, 066021 (2021).
[47] Y. Fang, R.-Z. Guo, and Q.-G. Huang, Phys. Lett. B **822**, 136654 (2021).

[48] R. Abbott *et al.* (LIGO Scientific and Virgo Collaborations), Phys. Rev. X **11**, 021053 (2021).
[49] R. P. Geroch, J. Math. Phys. (N.Y.) **11**, 2580 (1970).
[50] R. O. Hansen, J. Math. Phys. (N.Y.) **15**, 46 (1974).
[51] S. A. Teukolsky, Phys. Rev. Lett. **29**, 1114 (1972).
[52] S. A. Teukolsky, Astrophys. J. **185**, 635 (1973).
[53] P. Bueno, P. A. Cano, F. Goelen, T. Hertog, and B. Vercnocke, Phys. Rev. D **97**, 024040 (2018).
[54] H. Nakano, N. Sago, H. Tagoshi, and T. Tanaka, Prog. Theor. Exp. Phys. 071E01 (2017).
[55] N. Sago and T. Tanaka, Prog. Theor. Exp. Phys. 123E01 (2020).
[56] E. Maggio, M. van de Meent, and P. Pani, Phys. Rev. D **104**, 104026 (2021).
[57] L. F. L. Micchi and C. Chirenti, Phys. Rev. D **101**, 084010 (2020).
[58] L. F. Longo Micchi, N. Afshordi, and C. Chirenti, Phys. Rev. D **103**, 044028 (2021).
[59] S. Xin, B. Chen, R. K. L. Lo, L. Sun, W.-B. Han, X. Zhong, M. Srivastava, S. Ma, Q. Wang, and Y. Chen, Phys. Rev. D **104**, 104005 (2021).
[60] M. Srivastava and Y. Chen, Phys. Rev. D **104**, 104006 (2021).
[61] B. Chen, Q. Wang, and Y. Chen, Phys. Rev. D **103**, 104054 (2021).
[62] A. A. Starobinsky, Sov. Phys. JETP **37**, 28 (1973).
[63] S. Teukolsky and W. Press, Astrophys. J. **193**, 443 (1974).
[64] E. Maggio, A. Testa, S. Bhagwat, and P. Pani, Phys. Rev. D **100**, 064056 (2019).
[65] A. Buonanno and T. Damour, Phys. Rev. D **59**, 084006 (1999).
[66] W.-B. Han, Int. J. Mod. Phys. D **23**, 1450064 (2014).
[67] R. H. Price and J. Pullin, Phys. Rev. Lett. **72**, 3297 (1994).
[68] R. J. Gleiser, C. O. Nicasio, R. H. Price, and J. Pullin, Phys. Rev. Lett. **77**, 4483 (1996).
[69] Z. Andrade and R. H. Price, Phys. Rev. D **56**, 6336 (1997).
[70] G. Khanna, J. Baker, R. J. Gleiser, P. Laguna, C. O. Nicasio, H.-P. Nollert, R. Price, and J. Pullin, Phys. Rev. Lett. **83**, 3581 (1999).
[71] Q. Wang and N. Afshordi, Phys. Rev. D **97**, 124044 (2018).
[72] R. S. Conklin and B. Holdom, Phys. Rev. D **100**, 124030 (2019).
[73] S. E. Field, C. R. Galley, J. S. Hesthaven, J. Kaye, and M. Tiglio, Phys. Rev. X **4**, 031006 (2014).
[74] V. Varma, S. E. Field, M. A. Scheel, J. Blackman, D. Gerosa, L. C. Stein, L. E. Kidder, and H. P. Pfeiffer, Phys. Rev. Research **1**, 033015 (2019).
[75] L. Annulli, V. Cardoso, and L. Gualtieri, arXiv: 2104.11236.
[76] D. R. Brill and R. W. Lindquist, Phys. Rev. **131**, 471 (1963).
[77] D. A. Nichols and Y. Chen, Phys. Rev. D **82**, 104020 (2010).
[78] D. A. Nichols and Y. Chen, Phys. Rev. D **85**, 044035 (2012).
[79] N. T. Bishop, R. Gómez, L. Lehner, and J. Winicour, Phys. Rev. D **54**, 6153 (1996).
[80] N. T. Bishop, R. Gómez, L. Lehner, M. Maharaj, and J. Winicour, Phys. Rev. D **56**, 6298 (1997).
[81] J. Winicour, Living Rev. Relativity **12**, 3 (2009).
[82] C. Reisswig, N. T. Bishop, D. Pollney, and B. Szilágyi, Phys. Rev. Lett. **103**, 221101 (2009).
[83] J. Moxon, M. A. Scheel, and S. A. Teukolsky, Phys. Rev. D **102**, 044052 (2020).
[84] J. Moxon, M. A. Scheel, S. A. Teukolsky, N. Deppe, N. Fischer, F. Hébert, L. E. Kidder, and W. Throwe, arXiv: 2110.08635.
[85] S. W. Hawking and G. F. R. Ellis, *The Large Scale Structure of Space-Time*, Vol. 1 (Cambridge University Press, Cambridge, England, 1973).
[86] M. Sasaki and H. Tagoshi, Living Rev. Relativity **6**, 6 (2003).
[87] E. W. Leaver, Proc. R. Soc. A **402**, 285 (1985).
[88] Black Hole Perturbation Toolkit, http://bhptoolkit.org.
[89] R. M. Wald, Phys. Rev. Lett. **41**, 203 (1978).
[90] N. Loutrel, J. L. Ripley, E. Giorgi, and F. Pretorius, Phys. Rev. D **103**, 104017 (2021).
[91] M. Boyle, L. E. Kidder, S. Ossokine, and H. P. Pfeiffer, arXiv:1409.4431.
[92] R. H. Price and J. Pullin, Phys. Rev. Lett. **72**, 3297 (1994).
[93] A. M. Abrahams and R. H. Price, Phys. Rev. D **53**, 1972 (1996).
[94] Z. Andrade and R. H. Price, Phys. Rev. D **56**, 6336 (1997).
[95] G. Khanna, J. G. Baker, R. J. Gleiser, P. Laguna, C. O. Nicasio, H.-P. Nollert, R. Price, and J. Pullin, Phys. Rev. Lett. **83**, 3581 (1999).
[96] C. F. Sopuerta, N. Yunes, and P. Laguna, Phys. Rev. D **74**, 124010 (2006); **75**, 069903(E) (2007); **78**, 049901(E) (2008).
[97] C. F. Sopuerta, N. Yunes, and P. Laguna, Astrophys. J. Lett. **656**, L9 (2007).
[98] A. Le Tiec and L. Blanchet, Classical Quantum Gravity **27**, 045008 (2010).
[99] N. K. Johnson-McDaniel, N. Yunes, W. Tichy, and B. J. Owen, Phys. Rev. D **80**, 124039 (2009).
[100] C. W. Misner, Phys. Rev. **118**, 1110 (1960).
[101] J. M. Bowen and J. W. York, Phys. Rev. D **21**, 2047 (1980).
[102] J. G. Baker, M. Campanelli, and C. O. Lousto, Phys. Rev. D **65**, 044001 (2002).
[103] M. Campanelli, B. J. Kelly, and C. O. Lousto, Phys. Rev. D **73**, 064005 (2006).
[104] See https://www.black-holes.org/code/spec.html.
[105] M. Boyle *et al.*, Classical Quantum Gravity **36**, 195006 (2019).
[106] L. E. Kidder *et al.*, J. Comput. Phys. **335**, 84 (2017).
[107] N. Deppe *et al.*, `SpECTRE` v2022.01.03, 10.5281/zenodo.5815438 (2022).
[108] T. Mädler and J. Winicour, Scholarpedia **11**, 33528 (2016).
[109] R. Penrose and W. Rindler, *Spinors and Space-Time, Vol. 2: Spinor and Twistor Methods in Space-Time Geometry* (Cambridge University Press, Cambridge, England, 1984).
[110] M. Giesler, M. Isi, M. A. Scheel, and S. Teukolsky, Phys. Rev. X **9**, 041060 (2019).
[111] P. Mourier, X. Jiménez Forteza, D. Pook-Kolb, B. Krishnan, and E. Schnetter, Phys. Rev. D **103**, 044054 (2021).
[112] H. Lim, G. Khanna, A. Apte, and S. A. Hughes, Phys. Rev. D **100**, 084032 (2019).
[113] A. Dhani, Phys. Rev. D **103**, 104048 (2021).

[114] L. C. Stein, J. Open Source Software **4**, 1683 (2019).
[115] S. Ma, M. Giesler, V. Varma, M. A. Scheel, and Y. Chen, Phys. Rev. D **104**, 084003 (2021).
[116] N. Oshita, Phys. Rev. D **104**, 124032 (2021).
[117] F. Zhang, A. Zimmerman, D. A. Nichols, Y. Chen, G. Lovelace, K. D. Matthews, R. Owen, and K. S. Thorne, Phys. Rev. D **86**, 084049 (2012).
[118] R. Kubo, Rep. Prog. Phys. **29**, 255 (1966).
[119] D. J. A. McKechan, C. Robinson, and B. S. Sathyaprakash, Classical Quantum Gravity **27**, 084020 (2010).
[120] L. S. Finn and D. F. Chernoff, Phys. Rev. D **47**, 2198 (1993).
[121] J. Aasi *et al.* (LIGO Scientific and VIRGO Collaborations), Classical Quantum Gravity **32**, 115012 (2015).
[122] B. P. Abbott *et al.* (LIGO Scientific Collaboration), Classical Quantum Gravity **34**, 044001 (2017).
[123] C. Gundlach, R. H. Price, and J. Pullin, Phys. Rev. D **49**, 883 (1994).
[124] S. A. Hughes, Phys. Rev. D **62**, 044029 (2000); **67**, 089902(E) (2003).